

Review

# Towards In-Situ Geochemical Analysis of Planetary Rocks and Soils by Laser Ablation/Ionisation Time-of-Flight Mass Spectrometry

Marek Tulej <sup>1,\*</sup>, Peter Keresztes Schmidt <sup>1</sup>, Salome Gruchola <sup>1</sup>, Coenraad P. de Koning <sup>1</sup>, Kristina A. Kipfer <sup>1</sup>, Nikita J. Boeren <sup>1,2</sup>, Niels F. W. Ligterink <sup>1</sup>, Andreas Riedo <sup>1,2</sup> and Peter Wurz <sup>1,2</sup>

<sup>1</sup> Space Research and Planetary Sciences, Physics Institute, University of Bern, 3012 Bern, Switzerland

<sup>2</sup> NCCR PlanetS, University Bern, 3012 Bern, Switzerland

\* Correspondence: marek.tulej@unibe.ch

**Abstract:** Spectroscopic instruments were a part of payloads on orbiter and lander missions and delivered vast data sets to explore minerals, elements and molecules on air-less rocky planets, asteroids and comets on global and local scales. To answer current space science questions, the chemical composition of planetary rocks and soils at grain scale is required, as well as measurements of element (isotope) concentrations down to the part per million or lower. Only mass spectrometric methods equipped with laser sampling ion sources can deliver the necessary information. Laser sampling techniques can reduce the dimensions of the investigated sample material down to micrometre scale, allowing for the composition analysis of grain-sized objects or thin mineral layers with sufficiently high spatial resolution, such that important geological processes can be recognised and studied as they progressed in time. We describe the performance characteristics, when applied to meteorite and geological samples, of a miniaturised laser ablation/ionisation mass spectrometer (named LMS) system that has been developed in our group. The main advantages of the LMS instrument over competing techniques are illustrated by examples of high spatial (lateral and vertical) resolution studies in different meteorites, terrestrial minerals and fossil-like structures in ancient rocks for most elements of geochemical interest. Top-level parameters, such as dimension, weight, and power consumption of a possible flight design of the LMS system are presented as well.

**Keywords:** planetary exploration; in situ chemical analysis; chemical mapping; mineral crystallisation; LIMS; miniature mass analyser



**Citation:** Tulej, M.; Schmidt, P.K.; Gruchola, S.; de Koning, C.P.; Kipfer, K.A.; Boeren, N.J.; Ligterink, N.F.W.; Riedo, A.; Wurz, P. Towards In-Situ Geochemical Analysis of Planetary Rocks and Soils by Laser Ablation/Ionisation Time-of-Flight Mass Spectrometry. *Universe* **2022**, *8*, 410. <https://doi.org/10.3390/universe8080410>

Academic Editor: Jason P. Dworkin

Received: 13 June 2022

Accepted: 2 August 2022

Published: 4 August 2022

**Publisher's Note:** MDPI stays neutral with regard to jurisdictional claims in published maps and institutional affiliations.



**Copyright:** © 2022 by the authors. Licensee MDPI, Basel, Switzerland. This article is an open access article distributed under the terms and conditions of the Creative Commons Attribution (CC BY) license (<https://creativecommons.org/licenses/by/4.0/>).

## 1. Introduction

Knowledge of the chemical composition of planetary bodies is important in our understanding of the planetary system formation and contributes to the comprehension of the origin and evolution of the solar system [1]. Chemistry imposes important constraints on the current models of the origin and evolution of our solar system and is the key to understanding the physical and chemical conditions and processes that formed the first solids, planetesimals, planets and their moons.

Several space missions to rocky and outer planets, asteroids and comets have been conducted so far, performing chemical measurements from orbiting spacecrafts, landers and rovers. The characterisation of space instrumentation applied up to date for chemical analysis and how these instruments helped in the exploration of the planetary surfaces have been subject of two monographs, a few reviews and numerous technical papers dedicated to the mission payload and an individual instrument (e.g., [2–5]). The capabilities of the current space instrumentation allow the investigation of the mineralogical composition and measurements of a limited number of elements. The mineralogical composition of planetary surfaces was studied by means of electronic spectra in the visible and near-infrared regions using reflectance and emittance spectroscopy, and thermal infrared emission spectroscopy.

The global imaging studies of Mercury, the Moon, Mars, asteroids and Saturn's moons were conducted from orbit and surface analysis by multispectral imaging. The application of Mössbauer spectroscopy on Mars at the Gusev Crater and the Meridani Planum delivered complementary information on iron-containing minerals [6]. The element analysis of the surface composition was conducted almost exclusively by spectroscopic methods [4,5]. The Gamma-ray (GRS), X-ray (XRS) and neutron (NS) spectroscopic instruments were used on orbiting spacecraft and delivered element abundance distribution at the global scale. Lunar surface composition was investigated on Apollo 15/16 [7,8], SMART-I [9,10], Chang'E-1/E-2 [11], Kaguya (SELENE) [12,13] and Chandrayaan-1 [14]. The element composition of the surfaces of asteroids 433 Eros, Itokawa, Vesta and Ceres were analysed by the payloads on NEAR-Shoemaker, Hayabusa and DAWN spacecrafts, respectively [15–19]. Detailed chemical mapping of the Mars surface and Mercury were obtained with Mars Odyssey [20] and MESSENGER [21–23]. Direct measurements of the elements on a planetary surface were first conducted on the Moon by an Alpha Scattering Instrument (ASI) on the Surveyor 5–7 missions [24,25]. The 'Martian fines' were investigated with an X-ray fluorescence (XRF) instrument during the Viking missions [26] and with an alpha proton X-ray (APXS) instrument on Mars Pathfinder [27] and Mars Exploration Rovers (MER) [28]. On the follow up rover, Curiosity, mission to Mars, laser-induced breakdown spectrometer (LIBS) became part of the payload on the Mars Science Laboratory (MSL) [29]. The LIBS instrument at first was applied to investigate the element composition at the context level of 100  $\mu$ m micrometre size sample areas at target standoff distances from 1.6 to 7 m from the rover. It allowed also for the first time, the observation of minor and trace elements, including measurements of H, Li, F, and C elements, that were difficult to detect by the other space instruments [30,31].

The space instruments have obtained information on global and local surface mineralogy either by dedicated mineralogical instrumentation (optical, IR and Mössbauer spectroscopies) or derived from the element analysis of planetary materials delivered by nuclear, an X-ray and LIBS. Both methodologies that have been applied as complementary techniques were also helpful to recognise various mixed mineralogical phases [2]. Optical spectroscopic methods in the visible and IR spectral range were very useful in the determination of a variety of mineral phases e.g., pyroxenes, olivines, feldspars, iron silicate minerals, etc. Pyroxenes are among the most widespread rock-forming minerals in the solar system. They are an important proxy of magmatic processes on asteroids (e.g., Vesta) [32,33] or the thermal evolution of the Martian mantle [34]. These minerals are formed by crystallisation in magmatic processes, accompanying the cooling of planetary mantles. A rich array of secondary Fe-bearing minerals observed in some regions on Mars provided insight into the geological formations influenced by water–rock interactions [35]. The observation of differences in the pyroxene composition found in ancient highlands and later lavas, including deposits of ferroan anorthosite, were important findings for supporting the presence of an early lunar magma ocean. The Mössbauer spectrometers, being part of the payload on the Mars exploration rovers (MER) Spirit and Opportunity, delivered complementary information on Fe-mineralogical phases present on the plains of the Gusev crater and at the Meridian Planum regions, contributing to understanding mineral alteration via a hydrolytic and sulphatic mechanism [36]. By including the element composition of Ti, Al, K and O of the investigated surface into mineralogical analysis, a more detailed classification of lunar mare basalts could be achieved [37]. To determine the presence of pyroxene and olivine on asteroids, the abundances of seven elements (O, Si, Mg, Fe, Mn, Ca, and Na) also had to be measured [38]. The measurements of element abundances of (Al, Mg, Fe and Ti) in the lunar surface were used to probe magma concentrations and crystallisation and mineral formation processes. The radiogenic elements K, Th, U are incompatible and are concentrated in residual magmas as trace elements in the formed minerals. They are natural long-lived radioactive elements acting as a heat source of the igneous activity. The measurements of the distribution of these elements within different minerals provides the means to study the volatile inventory of a planetary body and yields insight into its initial temperature or impact history [39]. The studies of the

element abundances have been of help in the analysis of planetary salts and were found to be relevant to establish environmental conditions, which might be favourable for the development of life forms [40–42]. The Sample Analysis on Mars (SAM) on the Martian Science Laboratory (MSL) was designed to measure light elements (C, H, O, N, S) and isotope compositions using evolved gas and mass spectrometry [43].

The new programme for the space exploration, issued recently by the National Academies (USA) Space Group members in A Decadal Strategy for Planetary Science and Astrobiology 2023–2032, defines a number of currently unanswered problems in Space Science and proposes a number of investigations, which should be undertaken to help answering these questions [44]. The geochemical analysis should deliver information on the geological processes and transformations, which the planetary material has undergone, as well as yield insight into ancient environmental conditions, which could support past or present life. Among others, several in-situ investigations are recommended to study the various geological processes that were and still are shaping the planetary surface and to obtain information about their timescales. These challenging investigations would require much more sensitive measurements than current space instrumentation can deliver, including the quantitative measurements of trace elements and isotope compositions at least down to the part per million level. Particularly helpful would be the in-situ measurements of the trace elements and their isotopes, including lithophile (Rb, Sr, Cs, Ba), rare earth (REE), platinum group and field strength elements (Nb, Zr, Th, U), and radiogenic elements (via Sr-Rb, Pb-Pb, Pb-U schemes). The chemical analyses of planetary materials (mineralogical phase, grain or crystal) while conducted with high spatial resolution allow insights into material formation processes and geological transformations. This can be achieved from element and isotope systematics measured within mineral phases, grains and crystals. The information of chemical heterogeneity allows the critical assessment of the petrogenetic histories of rocks and characterisation of the geological transformations. Igneous minerals (e.g., olivine, plagioclase, pyroxene, apatite) and their inclusion records are particularly useful in the analysis of volcanic and magmatic processes, as they are an archive of these processes due to their intrinsic resistance to later rock transformation (e.g., weathering). The study of these minerals can deliver information of magma composition, temperature and open or close system processes involved in the transformation. Thus, the sources, processes and their timing in igneous magmatic systems can be elaborated from such data [45,46]. The studies of sedimentary rocks in addition to the characterisation of the environmental conditions, can be important in assessing planetary inhabitability. The geochemical analyses of the planetary body include the compositional details of the planetary surface and internal planetary structure. The primordial crust of rocky planets is typically formed from solidification of magma oceans and its composition can vary across planetary bodies (e.g., graphite on Mercury [47], olivine enriched deposits and spinel anorthosite deposits on the Moon, basalt and ultramafic magmas on Earth or Mars) and can be modified by secondary processes, e.g., volcanism or weathering.

In the current contribution we provide an update to the current status of our miniature LMS and its performance to conduct geochemical analysis. We review the results of several studies of different geological materials (meteoritic samples, igneous and sedimentary rocks) conducted by the miniature LMS system. These studies are of relevance to understanding planetary geochemistry and can also be conducted in situ on planetary surfaces. The results of the investigation of apatite (igneous rock) and zircon (lunar meteoritic sample) crystals are presented as examples how the LMS instrument would be used to obtain detailed insights into the volcanic and magmatic formation processes. In most magmatic systems, apatite crystallises at the early stage of lava cooling within a small temperature range and the crystals are well-preserved against later metamorphism and alteration processes [48]. Zircon is another important robust accessory mineral and one of the most stable minerals [49]. It is often investigated because its chemical composition yields information about complex geological histories. It is relevant as a mineral for age determinations and for zircon thermometry in high-grade metamorphic rocks and has the capacity to protect

mineral inclusions, the analysis of trace element patterns and to study their relation to the main mineral assemblages. LMS have reached the level that the geochemical studies can be conducted with spatial resolution down to micrometre levels. Whole-rock chemical analysis, although important to understand broad petrogenetic histories, produces chemical (element, isotopes) characteristics of average quality. Potential chemical variations within individual rock components are lost in this case and also frequently in the mineralogical context. Requirements for understanding the chemical composition on the micrometre-size grain level are necessary to study chemical heterogeneities and element systematics. Several studies were conducted by LMS on sedimentary rocks (silica chert) and carbonate rocks (calcite, aragonite) with high spatial resolution yielding information about element redistribution in micrometre-sized inclusion and the detection of putative fossils. We discuss the current performance of LMS to investigate mineralogical phases, elemental heterogeneities and isotope fractionations. The latter analysis can be particularly important in the investigation of dating and detection of bio-relevant processes.

## 2. Space Prototype Instrumentation Designed for In-Situ Chemical (Element, Isotope) Analysis

Mass spectrometers are necessary for the geochemical analysis. In addition to major elements and their isotopes, they can also measure trace element abundances down to the part per million and lower. High spatial resolution of the chemical sampling is another requirement and can be achieved by laser sampling methods. One of the new potential space-borne instruments is the CosmOrbitrap [50–53]. The instrument can conduct measurements with ultrahigh mass resolving powers of  $m/\Delta m \geq 100,000$  (full width at half maximum, FWHM) and ppm-level mass accuracy. It allows unambiguous identification of element (or molecular) masses within 3.2 ppm of absolute values [50–53]. Other space-born laser-based mass spectrometers are represented by laser ablation/ionisation time-of-flight mass spectrometers (LAMS [54], LAZMA [55], LMS [56]). They offer the direct sampling of solid materials by applying a laser ablation ion source, which produces atomic ions with concentrations proportional to the elemental concentration in the sample. Simple and robust instrument design and operation, high-speed measurements and high sensitivity and quantitative or semi-quantitative performance are achievable utilising of this instrumentation [57–61]. Several other space prototype instruments for in-situ chemical analysis have been developed as prototype for a specific applications, e.g., isotope dating. An example is the laser ablation-miniature mass spectrometer (LA-MMS), combining a laser ablation/electron impact ion source with double focusing mass analyser in Mattauch–Herzog configuration equipped with a CCD array ion detector [59]. With the material ablated from sub-millimetre sample spots, detection limits down to 0.4 wt.% were demonstrated. The instrument displayed accurate and precise measurements of the isotope ratios of K and Si. The Potassium–Argon Laser Experiment (KArLE) instrument was designed for dating applications under a NASA programme [60]. The instrument combines several flight-proven components, combining LIBS for the measurements of potassium concentrations and a quadrupole mass spectrometer for the Ar concentration measurements. The volume of the ablation crater is determined by optical microscopy. During performance testing KArLE attained accuracies of within 50 Ma for age determination [61]. Laser Desorption-Resonance Ionisation Mass Spectrometry (LD-RIMS) represents another instrument for accurate dating applications with a Rb-Sr dating scheme while being deployed on a rover [62,63]. The adaptation of laboratory techniques or the development of new space instruments with capabilities comparable to the ones of analytical laboratory instrumentation would be necessary to reach the required sensitivity levels and spatial resolutions [64,65]. The microscopic-sampling methods in laboratory practice employ laser ablation (LA) techniques, combined with inductively coupled plasma mass spectrometry (ICP-MS) or secondary ionisation mass spectrometry (SIMS). ICP-MS and SIMS are also common techniques applied in in-situ studies of isotope composition. A space-borne SIMS, the cometary secondary mass analyser (COSIMA), was used aboard the

Rosetta spacecraft to study dust particles [66]. Miniaturised ICP-MS instruments with a laser ablation source and potential for space mission application are presently not available but the developments are ongoing [67–69].

### 3. Laser Mass Spectrometer (LMS)

A miniature laser ablation/ionisation time-of-flight mass analyser (named LMS) system has been the subject of development in our laboratory over the last two decades [56]. After several improvements and upgrades of the ion optical system, detection and acquisition systems, and improvements of the measurement protocols, the current instrument can be applied to a sensitive analysis of soils and rocks [70–73]. The surface chemical imaging and 3D chemical analysis by adding depth profiling measurements can be conducted routinely with sensitivity down to a few parts per thousand (per mil) levels, a few micrometre lateral and sub-micrometre vertical resolution [74–79]. LMS demonstrated its high performance for the chemical analysis of micrometre-sized objects, such as mineralogical grains, layers, biologically relevant films and microscopic fossils [80–83]. The measurement protocols allowed more accurate measurements of the isotope abundance and the improvements of overall chemical composition quantification [84–88].

Figure 1a shows schematic diagram illustrating the principle of operation of the LMS instrument. A focused laser radiation is used to remove a thin layer of material from the surface. The laser ion source parameters (e.g., pulse energy, radiation wavelength) are tuned in such a way that atomisation and ionisation of the sample material is close to atomic stoichiometric ratios as they are present in the material and the atomic concentrations reflect the element concentrations of the removed surface layer. To improve the quantitative performance of the measurement, one can conduct, in parallel, a measurement on standard research material (SRM) to obtain relative sensitivity coefficients (RSCs) and correct for the different ionisation yields of elements at the applied laser ablation ion source conditions [89]. The atomic ions formed in the ablation process are temporally and spatially separated, according to their mass to charge ratio by a time-of-flight (TOF) mass analyser and recorded by the ion detector (multichannel plate, MCP) as a function of time of arrival into the detector. This is arranged by an ion optical system, which confines, focusses and transmits the ions from the ablation spot through the field-free region, reflectron and field-free region again to an MCP ion detector. The photograph of the mass analyser is shown in Figure 1b, also indicating the typical dimensions of the mass analyser without the laser optical system. Figure 1c shows a possible schematic of the laser mass spectrometer for space application (see also [58]). The dimension of a compact instrument, combining mass analyser, laser optical system with a microchip laser, including instrument compartment, are about 400 mm × 200 mm, an instrument weight of about 13 kg, with an average power consumption of about 45 W (all electronics included). These parameters can be further optimised to meet the technical requirements on a rover or a lander platform. Currently, miniature pulsed laser systems are available commercially. Nevertheless, these systems are typically ns- or sub-ns lasers. Miniature fs-laser systems are not available until now but with progress in fibre technology miniaturization of these systems is also expected in near future.

The mass analyser delivers multi-elemental composition information of the ablated surface layer and interrogated surface area/volume for each applied laser pulse. The mass spectrometric analysis involves transformation from the time scale to the mass scale to assign measured mass ion peaks to the corresponding elements (isotopes). The mass peak integration in the time spectrum yields the number of measured ions, and the measurement of all atomic ions provides the means to derive the atomic and isotope concentrations, respectively. The detailed procedure used for the analysis of the mass spectra can be found in our previous publication together with the evaluation of the accuracies of the applied methods [84]. Although the instrument is capable of measuring almost all elements with the exception of rare gas elements, its sensitivity can vary depending on the laser ablation ion source parameters, including laser pulse duration, radiation wavelength, pulse energy,

laser irradiance and fluence, and physical and chemical material properties [87]. These so-called measurement fractionation effects can be generally minimised by selecting a short laser pulse duration (preferably femtosecond laser pulses) and a short laser radiation wavelength (preferably in the UV or VUV spectral range) at sufficiently high laser pulse energy and irradiance [89]. The LMS instrument has an optimised ion transmission close to 100%, thus the fractionation effects due to the mass analyser are considered to be negligible [56]. The current LMS system allows sensitive studies on geological samples and quantitative or semiquantitative chemical composition analysis, depending on if in parallel relevant standard materials are used or not [88,89]. Owing to the typically observed dynamic range of about  $10^5$ , detection limits of ten (or better) ppm (parts per million) in atomic fractions can be achieved depending on the efficiency of the atomic ionisation [57,73,88,89]. The quantitative element analysis can be delivered down to ppm levels [29,88]. Improved detection capabilities can be further achieved with a multi-anode detector system and by applying a high voltage pulser to hinder atomic ions with the highest concentrations from reaching the detector [71,90,91]. The measurement of isotope concentrations is a unique capability of the LMS instrument. Our studies show that the accuracy and precision of the isotope abundance determination depends on the isotope concentration (atomic fractions) and can be at per mil level if the isotope concentrations are larger than 10–50 ppm [59,92]. Further improvements to the accuracy and precision of the isotope ratio determination was achieved by applying the isotope intensity correlation method and spectra filtering [85,86]. Our studies have demonstrated sufficiently high accuracy and precision in the determination of the Pb, S and Ni isotope ratios so that isotope fractionation effects can be examined for Pb-Pb dating (both accuracy and precision at a few per mil level) [92], biologically relevant fractionation of the S isotopes (both accuracy and precision at per mil level) [93], or both bio-relevant or geological fractionation of the Ni isotopes (both accuracy and precision at per mil level) [86].

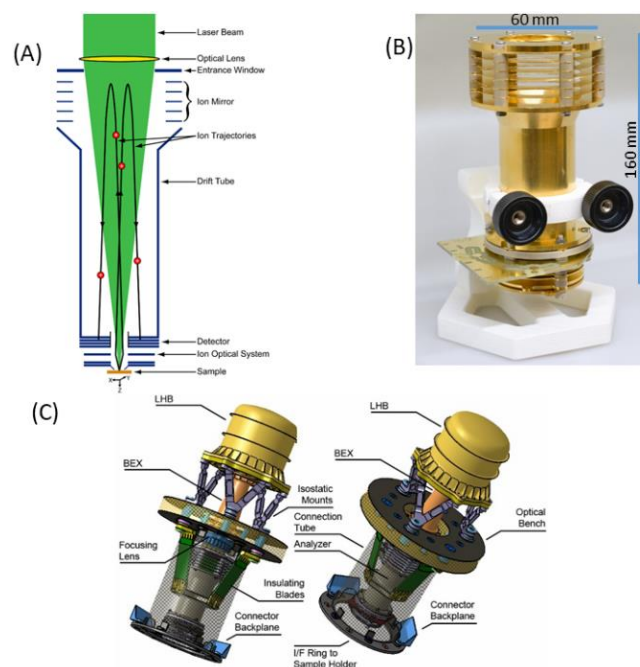


**Figure 1.** Schematic diagram of a miniature LMS with key parts labelled (A), an image of the mass analyser with its dimensions (B) and a possible design of a space instrument with an optical part (optical system with a microchip laser) attached to an optical bench (interface), introducing a focused laser radiation from the reflectron site (C).

Sub-micrometre vertical and micrometre lateral spatial resolution can be maintained with the control of laser ion source parameters (flexible focussing optics, laser pulse energy

tuning) [94–96]. The measurements can be performed on raw samples and do not require the application of advanced surface preparation methods. Very recent reviews describe the current progress in development of various LIMS systems, also providing details of the design and operation, as well as reviewing numerous LIMS studies on geological, meteoritic and biological samples along with applications to material science conducted by groups developing LIMS systems [87,97].

Through chemical surface mapping, one can analyse many locations experimentally, which provides a large number of mass spectra frequently exceeding the 10 000's. The identification of compounds in the measured spectra involves statistical analysis. Several earlier studies applied supervised machine learning principles for the rapid identification of microorganisms [98] or tumour [99] from mass spectrometric data collected in the chemical imaging of the sample surface. Recently, we have introduced unsupervised data reduction methods capable of recovering groups of spectra that share a significant level of similarity [100]. The mass spectra encode the necessary information about microscopic structures, minerals, chemical compounds and other heterogeneities within the surface, but due to the high dimensionality of the analysis problem, with each additional mass adding one dimension, the direct mass spectrometric analysis is laborious. Applying dimensionality reduction (PCA, SVD) and manifold learning techniques (e.g., UMAP, t-SNE), one can capture essential data patterns based on their spectral similarities. This analysis method is based on the principle that spectra recorded from the same chemical compound are similar, whereas spectra recorded from different chemical compounds, for example two different minerals, will share only little to no similarity. The data can, therefore, be grouped into clusters of spectra with a similar chemical fingerprint. One can visualise these relationships by embedding the dataset into a low dimensional space, e.g., 2D or 3D, and representing each spectrum with a node. Similar spectra will be embedded close to each other; hence, for each chemical compound present in the dataset a cluster will be formed. Using clustering algorithms (e.g., DBSCAN, HDBSCAN) the different clusters can be retrieved from the embedding, and labels can be assigned to the spectra, according to which cluster they belong to. Instead of analysing the dataset as a whole and trying to identify different compounds, one can now simply analyse the data from each cluster individually through basic spectrum analysis, which allows us to identify the corresponding compounds and, therefore, determine the composition of the investigated sample. This method is a great tool for geological samples to identify different mineral phases but can in principle be applied to any data obtained from different compounds, as long as the spectra contain more or less pure contributions from only one of the present compounds (no mixtures).

The method was successfully applied to the Gunflint chert, a 1.88 Ga quartz sample hosting remnants of Precambrian microbes in the form of microfossils [101,102]. Three distinct clusters were retrieved, which were later identified as the quartz cluster, the microfossils cluster and a third cluster containing spectra from inclusions with higher metallicity. LMS is capable of recording the chemical signatures of microfossils in geological samples, and by applying spectral similarity clustering the interesting spectra can be quickly identified even in large datasets.

While comparing with the other space and space prototype instrumentation designed for elemental analysis, LMS offers several advantages and improvements. Like LIBS and COSMORBITRAP instruments, LMS can be used for a rapid remote analysis without sample preparation. The current LMS instrument offers increasingly higher sensitivity and element detection limits down to ppm or better and can be used to measure the accurate isotope concentrations of several elements. Contrary to LIBS, LMS requires a dedicated vacuum system for the mass analyser operation and ion detector system when the investigations would be conducted on Mars. With a time-of-flight mass analyser, all atomic ions can be measured for each applied laser pulse allowing for robust multielement measurement capabilities. In the present applications, the fast data acquisition cycle allows measurement of 1000 spectra per second. However, owing to the limited mass resolution ( $m/\Delta m = 500$ ),

the isobaric interferences, due to the presence of the isotope of other elements or molecular clusters, cannot be resolved directly contrary to the COSMORBITRAP instrument. However, the contribution due to other atomic isotopes can be derived by considering the natural isotope composition, and the possible influence due to isobaric clusters can be inferred from the overall cluster appearance in the mass spectrum. To reduce these latter contaminations, a double pulse laser ablation/ionisation ion source was introduced, where after the first laser pulse used for the sample ablation, a second pulse is applied to heat up the generated plasma plume and reduce post ablation plasma chemistry and cluster production [70].

High spatial resolution chemical imaging and depth profiling analysis down to micrometre level is routinely demonstrated by LMS and can, in principle, also be achieved with other instruments. By employing a microscope camera system in parallel to the LMS measurements, context surface imaging of the areas around the investigated spots can be recorded, helping with the interpretation of the mass spectrometric results and allowing for an improved analysis of physical and chemical properties of the surface [60].

#### 4. Geochemical Analysis with LMS

A short summary of the mass spectrometric studies of a few geological materials listed here serves as examples of possible investigations, which could be carried out on planetary surfaces with the current space-borne mass spectrometric instruments, including our laser mass spectrometer LMS. Several geochemical analyses conducted with LMS demonstrate the capabilities of the instrument to investigate element heterogeneities and contribute to the normative mineralogy of meteoritic samples, trace element analysis in apatite crystal and zircon grains, and contribute to the identification of element zoning and magma cooling mechanisms and the determination of the crystallisation temperatures and dating. Finally, the instrument is also capable of measuring micrometre-sized inclusions, putative microscopic fossils and stromatolite films in the sedimentary rocks and contribute to the characterisation of the ancient environments, characterisation of biosignature and the effects of weathering and mineral transformation (calcite carbonate, aragonite and silica chert).

##### 4.1. Meteoritic Samples

###### 4.1.1. Allende

The Allende meteorite is composed of carbonaceous chondrite material irregularly shaped white calcium aluminium inclusions (CAI) and rounded chondrules in a dark matrix. The CAI are composed of minerals, which are believed to have condensed at high temperatures. The mass spectrometric studies were conducted initially at 138 locations on the Allende sample surface. The concentrations of numerous elements, including C, Mg, Al, Si, S, Ca, Sc, Ti, V, Cr, Mn, Fe, Co and Ni, were determined in these studies. The concentrations of the mineral forming elements Mg, Si, Fe, Ca and Al were observed to vary within 10 % between different locations, and variations of elements Ti, V, Ni and Sc were significantly larger. The latter are refractory elements preferentially contained in refractory chondrules. Furthermore, an enrichment in the lithophile elements Ca, Al and Ti, compared to the siderophile elements Co and Ni and compared to CI chondrites could be observed [74]. The matrix material was observed to be depleted in volatile elements. In follow up studies on the Allende matrix composition, the concentration of C, O, S, Na, K, Li, Mn, P, Cr, Si, Fe, Mg, Ni, Co, V, Ca, Ti, Al and Sc elements were measured together with their spatial variability on different scales from 50  $\mu\text{m}$  to 0.5 mm [103]. With the results obtained from the measurements at 1651 locations, the presence of an olivine-rich composition for the matrix was determined by analysing the  $n(\text{Si})/(n(\text{Mg}) + n(\text{Fe}))$  dependence, where  $n(\text{X})$  denotes the concentration of element X. In addition, the components of Mg-Fe-rich minerals could be identified and the analysis around the chondrules location indicated the presence of grain-sized minerals with higher  $n(\text{Si})/(n(\text{Mg}) + n(\text{Fe}))$  ratios than measured for the matrix material, and some individual Al-rich analyses. The olivine in the Allende matrix was found to have nearly equal amounts of forsterite and fayalite, with only a small

shift towards Fe-rich olivine [103]. A high degree of chemical homogeneity of the matrix implies that it formed independently from, or in parallel with, the chondrules and that the process that led to the formation of the parent planetary body was a fast collapse of the dust–gas cloud following chondrule formation.

#### 4.1.2. Lunar Meteorite Sayh al Uhaymir 169 (SaU169)

The SaU169 meteoritic materials were found in 2002 in Oman. SaU169 consists of two different lithologies: holocrystalline, a fine-grained polymict impact-melt breccia makes up around 86% of the rock volume (enriched in K, REE and P elements) and the remainder is shock-lithified regolith breccia [104]. The LMS system was used to perform chemical mapping analysis to understand the chemical heterogeneities across the surface [75]. From the mass spectra obtained from the fine-grained matrix area, high abundances of Li, Na, K, O, Mg, Al, Si, K, Ca, Ti and Fe elements were measured, which are common in many rock-forming minerals. The analysis identified a zircon grain within the analysed surface area by means of a distinct element composition with the (Zr, O and Si) mass peaks being the most intense in the measured mass spectrum [75]. The analysis of the mass spectra recorded within the zircon grain ( $ZrSiO_4$ ) area show the presence of a few heavier elements, such as Hf, Y and several rare earth elements (REE), including Yb, Dy, Gd and Er. Furthermore, more common cations in silicate minerals, such as Na, K, Mg, Al, and Fe, were measured at the trace level with concentrations corresponding a few tens of ppm. They are typically identified as the impurities in zircon crystals. The chemical compositions of individual spot analyses was further investigated by plotting them on ternary diagrams (Figure 2). The majority of measurement points have element ratios close to the nominal composition of zircon. Red spots outside this area were found to be close to the rim of the zircon grain, where other minerals are also present. The surrounding matrix material consists mainly of pyroxene (ortho- and clinopyroxene), plagioclase (anorthite-rich), K-feldspar, as well as some ilmenite. Most of the measurements were conducted on the mixture of several minerals. The data points for these analyses, therefore, lie between those of the end-member minerals.

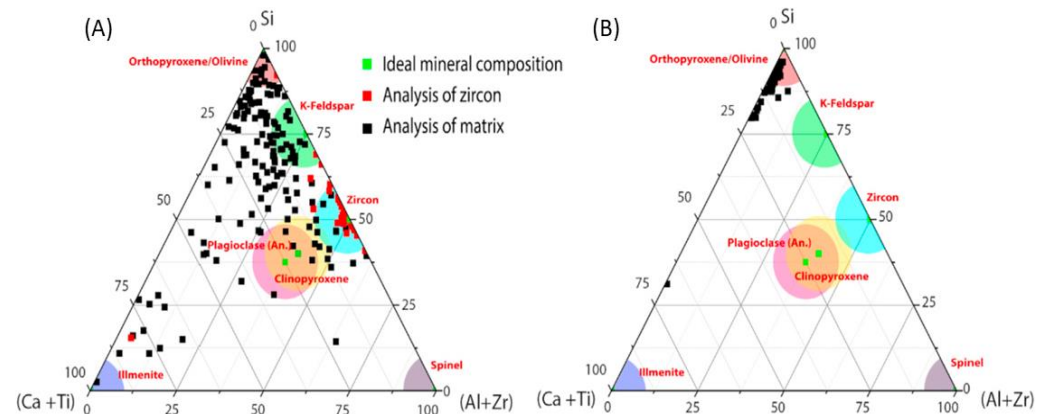


**Figure 2.** Ternary diagrams to visualise the minerals present in the sample: (A) Area containing a zircon grain on the KREEP-rich sample; (B) Area on the border between the KREEP-rich and regolith parts of the meteorite (Reproduced with the permission from the journal Planet. Space Sci. [104]).

The mass spectrometric results were used to determine the crystallisation temperature of zircon. The abundance of Ti in one zircon grain was measured in 56 locations. With the available data set, the zircon crystallisation temperature was investigated using the method of Ferry and Watson yielding a range between 850 to 1450 K, with an average temperature of 1176 K and a variance of 140 K [105]. Due to its unique chemical and physical durability, zircon found in rocks has to be placed in a geological context. In the current case, the Ti concentrations in zircon correlate well with the temperature at which the grain originally crystallised, and the result was found to be consistent with the scenario that

the analysed grain has been formed in a slowly cooling and evolving melt when it reached zircon saturation. With the abundances of U and Pb in the zircon grain, an approximate zircon crystallisation age of  $(3517 \pm 130)$  Ma was determined in this study.

#### 4.2. Sedimentary Rocks

##### 4.2.1. A mineralogical Inclusions in Calcite Carbonate

Three-dimensional composition information and oxidation properties were investigated on a mineralogical inclusion embedded in a colourless amygdale of calcium carbonate. A dark inclusion resembled a tangle of filamentous structures outward propagating in all directions was visible using an optical microscope, and tomographic reconstructions Figure 3a,b showed characteristic millerite (a NiS mineral commonly associated with serpentine rocks) structure [80]. Small denser grains can also be seen both within the inclusion and in the surrounding calcite. The chemical depth profiling studies were conducted across the inclusion area and yielded the chemical composition variation along approximately 30  $\mu\text{m}$  deep material thickness. The presence of oxides and sulphides of various elements, e.g., Mg, Ti, Mn, Fe, Ni and Co within the inclusion material served as the internal calibration standard to derive elemental abundance calibration factors (relative sensitivity coefficients, RSCs) for major and minor elements. With increasing distance from the host phase towards the inclusion centre, an increased content of oxygen was measured. Oxides and sulphides of several metals were observed as separate entities but some of the metals could fill the sites of complex mineralogical compounds. Depth profile analysis delivered compositional details on in-depth elemental concentration variabilities with the presence of distinct grain and mineralogical layers re-distributed around the millerite crystals. The sub-micrometre vertical and about 15  $\mu\text{m}$  lateral resolutions of the depth profiles were sufficient to study chemically distinct micrometre-sized objects, such as mineralogical grains and thin layers of minerals, including micrometre-sized filamentous structures of millerite (Figure 3). The mass spectrometric analysis, which display element correlation on the ternary element correlation graphs, combined with the Raman spectroscopic studies led also to the conclusion that the dark inclusion is a highly weathered basalt with olivine, and pyroxene (augite) phenocrysts with a dominating amygdales phase [80,81]. The results of the LMS investigations were combined in ternary plots to identify mineralogical phases present in this sample (Figure 4). Amygdales in basaltic lavas are formed after lava cools down and hydrothermal fluids fill the cavities followed by secondary minerals formation after the hydrothermal fluids precipitate as a bubble.

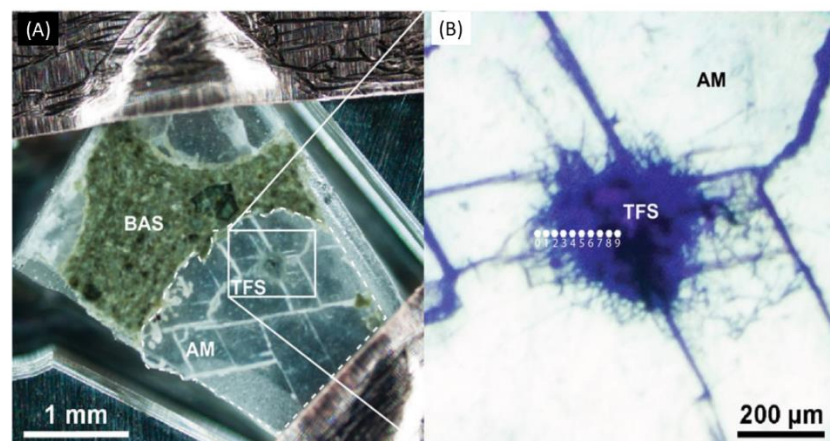


**Figure 3.** Optical images showing the (A) entire sample including the host basalt (BAS), the amygdale (AM) and the tangle of filamentous structures (TFS) and (B) placement and numbering of the points investigated by LMS in the dark inclusion resembling a TFS [80].

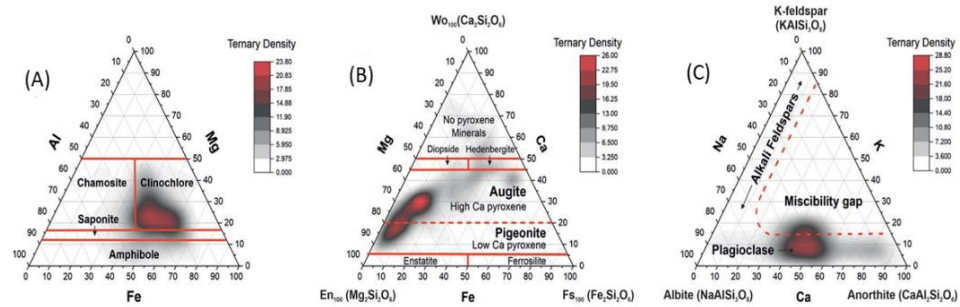


**Figure 4.** Ternary plots of the elements relevant (A) chlorite group; (B) magnesium augite and pigeonite; (C) the plagioclase feldspars in the inclusion material. (Reproduced with the permission from the journal *J. Anal. At. Spectrom.* [81]).

#### 4.2.2. Micro-Sized Inclusions in Aragonite Crystal

Chemical composition mapping and depth profiling studies at the interface between the aragonite veins hosted in serpentinitised harzburgite were conducted on dark filamentous micrometre-structures enclosed about 54,900 a ago [106]. The mass spectra recorded on the filamentous structures delivered a distinctly different chemical composition compared to that of the aragonite ( $\text{CaCO}_3$ ) host matrix. Several major (O, Na, Mg, K, Ca, Mn, Fe, and Co), minor (C, Si, S, Cl) and trace elements (B, N, F, Al, P, Ti, Cr, and Ni) were measured in the filamentous material. The chemical mapping and depth profiling was applied to isolate filamentous microstructures from the host mineral phase by means of the distinctly different mass spectra, followed by the mass spectrometric determination of the element concentrations. The detection of biologically relevant elements (B, S, Mn, Co, Fe and Se) in the material indicated a possible bio-origin of the investigated filaments. A few other minor elements, including B, F, and Cl, although also important in biologically relevant processes, were likely the remnants of the ancient ocean at the time of aragonite enclosure. Follow-up chemical analysis of the putative fossils was aimed at the determination of possible isotope fractionation effects of B and Ni isotopes, due to the geochemical and/or bio-relevant processes [86]. The Ni isotope values were measured on a Ni standard research material, indicating an accuracy and precision at sub-per mill level. The studies on trevorite mineral led to the determination of  $\delta^{60}\text{Ni} = (-0.30 \pm 0.16)\%$ . This accuracy and precision is still outside the range of  $\delta$ -values, which are required for the assignment of this rock either to bulk silicate  $\delta^{60}\text{Ni} = (0.05 \pm 0.05)\%$  or ultramafic  $\delta^{60}\text{Ni} = (-0.3 \text{ to } +0.2)\%$  [107]. The Ni isotope ratio analysis on the filamentous structures (putative microscopic fossils) yielded a mean value for  $\delta^{60}\text{Ni}$  of  $(-3.32 \pm 0.81)\%$ , which is significantly larger than expected from the geochemical fractionation effects and somewhat larger than expected typically for the bio-relevant fractionation (Figure 5). Commonly applied C- and S-isotope biosignature analyses should help to better understand the nature of the filamentous structures. For B, a mean value of  $\delta^{11}\text{B} = (-46.1 \pm 2.9)\%$  was derived that corresponds to a ratio of  $^{11}\text{B}/^{10}\text{B} = 3.84 \pm 0.68$ , which was found within the range of terrestrial ratios (4.03) but the accuracy and precision of this study should be improved for detailed environmental applications. These results can further improve by focusing only on the dedicated isotope analysis at increased signal-to-noise ratio (S/N). This can be arranged by removing other atomic ions than the ones of interest from the analysed ion bunches using a high voltage pulser within the time-of-flight mass analyser and the application of a double pulse ablation/ionisation method [71,73].

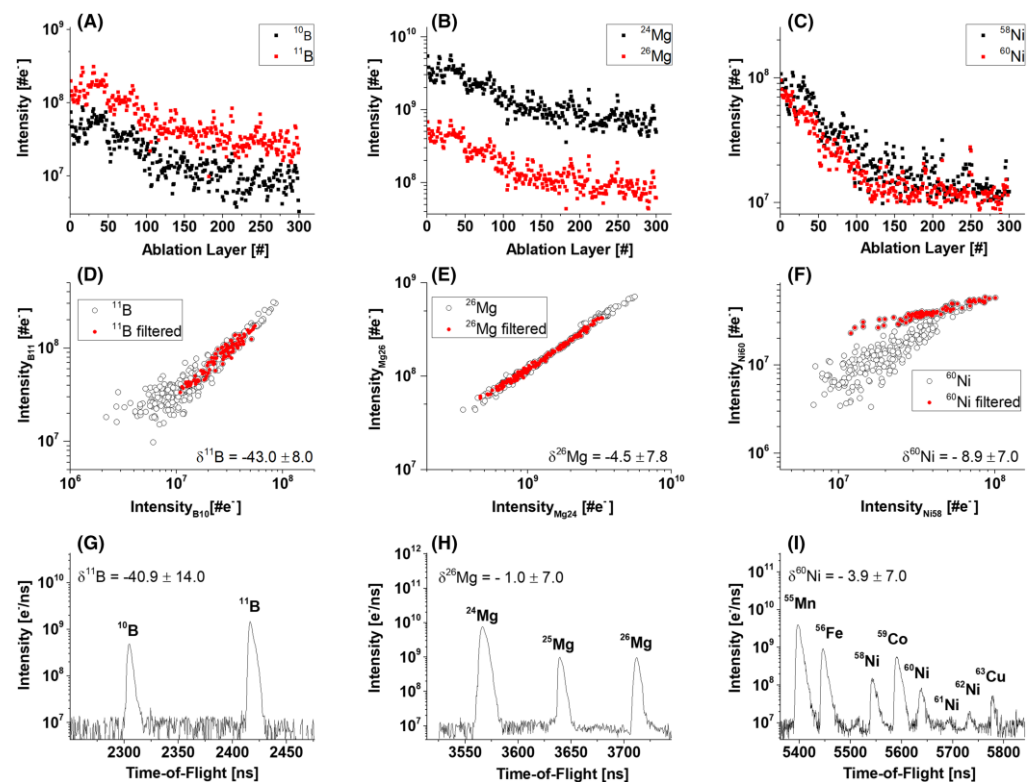


**Figure 5.** Panels (A–C) show depth profiles for the B, Mg and Ni isotopes at the location of a dark, micrometre-sized inclusion in the aragonite sample. Panels (D–F) show the isotope intensity correlations as raw data points (open circles) and after spectra filtering (full circles). Panels (G–I) show sections of the recorded time-of-flight spectra of the elements B, Mg and Ni with their isotopes. (Reproduced with the permission from the journal *J. Mass Spectrom.* [86]).

#### 4.2.3. Micro-Sized Inclusions in Silica Chert

Precambrian chert from banded iron formations (Gunflint formation, 1.9 billion years old) was investigated with LMS and optical spectroscopy [101,102,108]. Chemical surface mapping and depth profiling were applied to identify microscopic fossil materials for mass spectrometric analysis. The Gunflint silica chert is considered to be an astrobiologically relevant Mars analogue considering possible precipitation of iron oxides and silicates to an aqueous mineral phase from an Fe- and Si-saturated water column while efficiently trapping any microbiota present in such environment [109]. The chemical composition of microscopic inclusions within the chert could be characterised at precisely defined locations and depth positions. The identification of the microscopic fossils and the quartz matrix was performed with (C, Si, and O) elements, analysing their concentration in the depth profiles. The main elements identified within the silica matrix and microfossils were (Si, O, Na, K, H, and Ca) and (Li, B, N, Mg, Cl, P, S, Ti, V, Mn, Fe, Cu, Ni, La, Ce) with strongly enhanced C and H compared to the host mineral. By applying weighted mass correlation networks, isotope ratios, and the projection of intensities into the low dimension using principal component analysis (PCA), unique compositional details of the microscopic fossils and minerals were investigated with new insights into the distribution, preservation, and element speciation of the microscopic fossils (Figure 6) [102]. Further extended data analysis utilizing topological details of the spectra distributions allow us to distinguish preserved microscopic fossils from organic contamination and inorganic host mineralogy. The topological analysis involved the application of the uniform manifold approximation and projection (UMAP) algorithm. The classification of the scores was prepared with a hierarchical density-based clustering algorithm (HDBSCAN) and visualised by the Mapper algorithm [102].

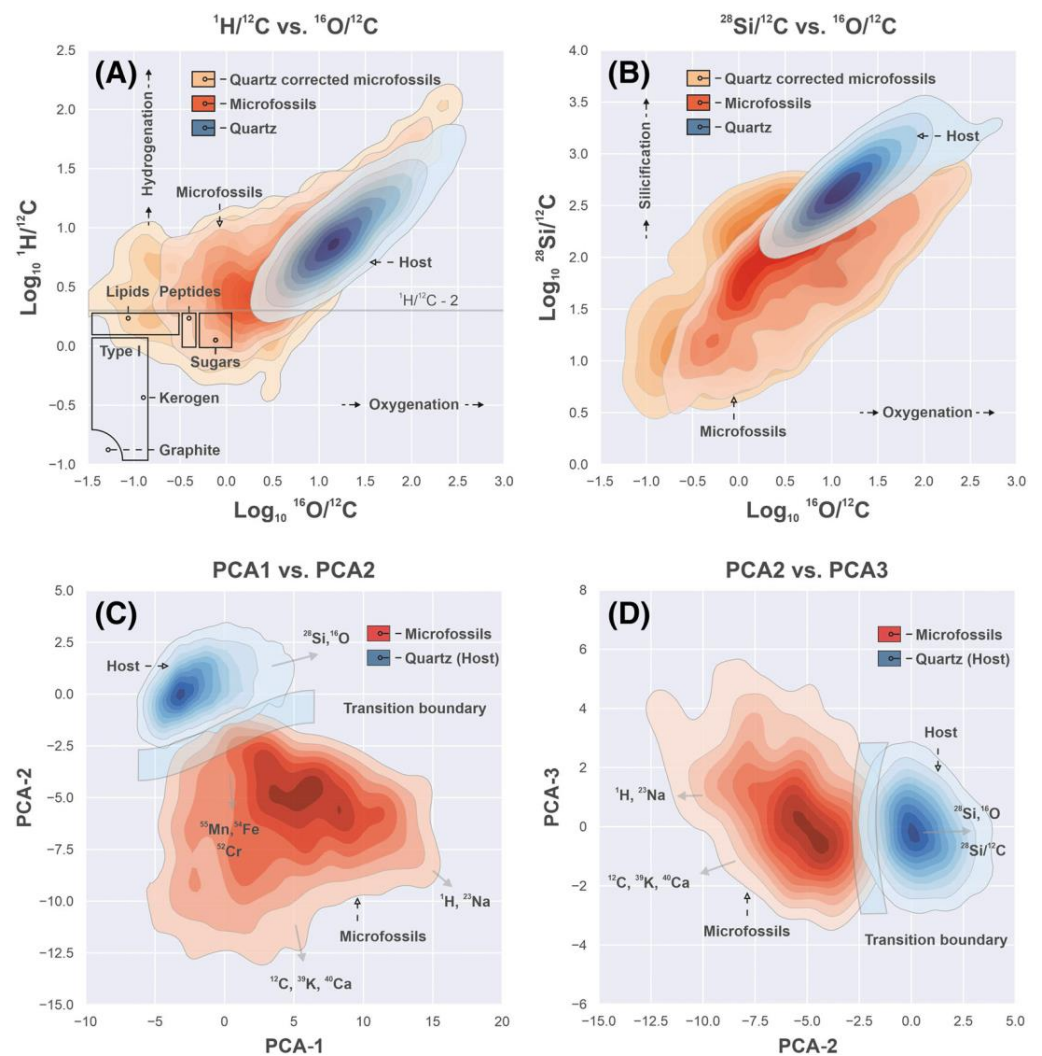


**Figure 6.** The mass spectrometric data can be separated into the data characterising mineralogical host phase and fossilised entities with their specific chemical compositions. (A,B): Kernel density estimates (KDE) of  $^1\text{H}/^{12}\text{C}$  and  $^{28}\text{Si}/^{12}\text{C}$  as function of  $^{16}\text{O}/^{12}\text{C}$  ratios, respectively (Van Krevelen plots). Blue and red kernels represent values measured from the host and microscopic fossilised areas, respectively. (C,D): 2D projections of the 196 features into the principal components space. Arrows represent loading directions for different single unit masses. The blue transparent line indicates the location of the transition boundary between two classes. (Reproduced with the permission from J. Chemometrics [102]).

### 4.3. Apatite Crystal in Igneous Rocks

Apatite is ubiquitous albeit a frequently low abundance mineral in most igneous rocks. Its common presence is accounted for by low solubility in naturally occurring melts and aqueous solutions and the limited ability of common rock-forming minerals to accommodate phosphorus into their structure. As an accessory mineral in igneous and other rocks, it commonly contains a range of elements that do not fit well into the major rock forming minerals, such as rare earth element (REE), and become a suitable target for investigating physical and chemical conditions in igneous rocks and the volatile evolution of magmas, hence, igneous petrogenetic processes and their modelling [109–113].

Apatite is a calcium phosphate mineral expressed by the chemical stoichiometric formula  $[\text{Ca}_{10}(\text{PO}_4)_6(\text{X})_2]$ . The halogen site, X, is occupied by  $\text{F}^-$ ,  $\text{Cl}^-$ , and  $\text{OH}^-$  corresponding to an isomorphous series with fluor-, chlor- and hydroxyl-apatite end members, respectively. The apatite investigated with LMS is a fluorapatite mineral isolated from an

ultramafic phosphorite rock from the Phalaborwa Complex (Limpopo Province, South Africa) formed 2.06 Ga ago (in Paleoproterozoic) [114]. Several previous studies have revealed the element partitioning and magmatic sourcing and hypothesised on the magmatic and post-magmatic mineral evolution in this region [46,114–118].

The chemical composition of the apatite sample was measured with high spatial resolution (10  $\mu\text{m}$  spot size, sub-micrometre depth resolution) on 900 locations covering a sample area of  $0.9 \times 0.9 \text{ mm}^2$  (Figure 7). The photomicrograph shows the investigated area in more detail. Location 1 marks a mineralogical phase that is in contact with the apatite crystal via a rim (location 2). Location 3 is tentatively assigned to the crystal core. Furthermore, at locations 4, 5 and 6, coloured reflections can be noticed at the micrometre size dimensions. The image also indicates the presence of several apatite crystal sheets. In the mass spectra obtained for the apatite crystal, the (O, F, Ca, P and Cl) elements are observed as major elements as expected for fluorapatite. A number of trace elements, including C, Na, Mg, Si, S, Cl, K, Mn, Fe, Sr, Ba and LREE (La, Ce, Pr, Sm), were measured at abundances levels down to part per million (atomic fractions). An anomalous increase in the element concentrations was observed at locations 4 and 5 for Sr and B and at location 6 for Th and U.

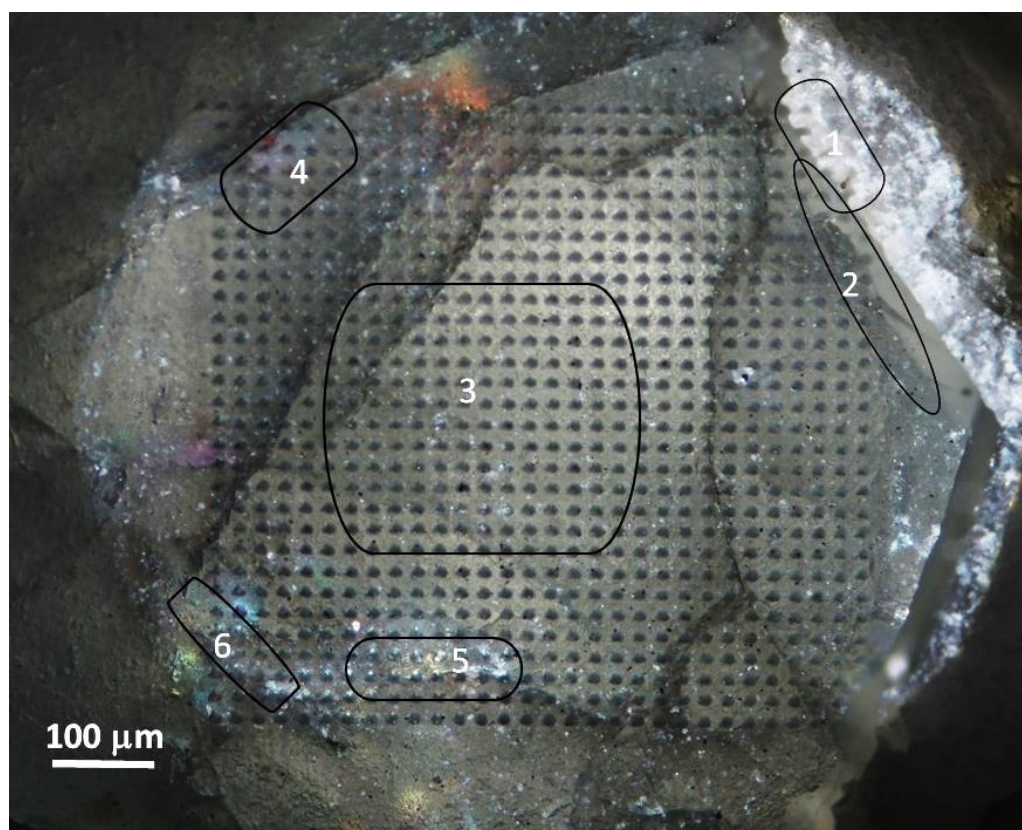


**Figure 7.** A microscope image of the apatite crystal surface along the z-axis with several crystalline sheets. On the left side the crystal is in contact with carbonatite rock (location 1) through a rim (location 2). The crystal core area (location 3) is surrounded by regions with enhanced abundances of (Th, U) at location 4, and Ba at locations 5 and 6.

440 mass spectra were recorded at a single location and yield chemical information about an ablated layer. By plotting the element intensities, one obtains intensity of the elements along the crater depth. Figure 8a shows the results of depth profiling analysis prepared for the major elements: O, Ca, P, Cl, and F. The element intensities are observed to decrease monotonically in a characteristic fashion observed typically in laser ablation studies by applying Gaussian laser beam profile. The intensity correlation curves of Ca, F,

P with O prepared on the depth profiling data indicate negligible depth heterogeneities (Figure 8b) [96]. The intensities are linearly correlated with a Pearson coefficient larger than 0.98 and with the slope coefficients close to stoichiometric values expected for the apatite mineral. Figure 8c displays the measured intensity correlation between (Cl, H) and F. Whereas the Cl intensity correlates well with the F intensity, the correlation between the H and F intensities is weak with a Pearson coefficient of  $R^2 = 0.50$ . The depth profiling analysis of H indicates that the H concentration is much larger at the surface and decreases with a much higher rate of depth than other elements. This observation indicates that the measured H concentration is rather a contamination due to the atmospheric water adsorbed at the uppermost apatite surface layers than OH in the apatite crystal.

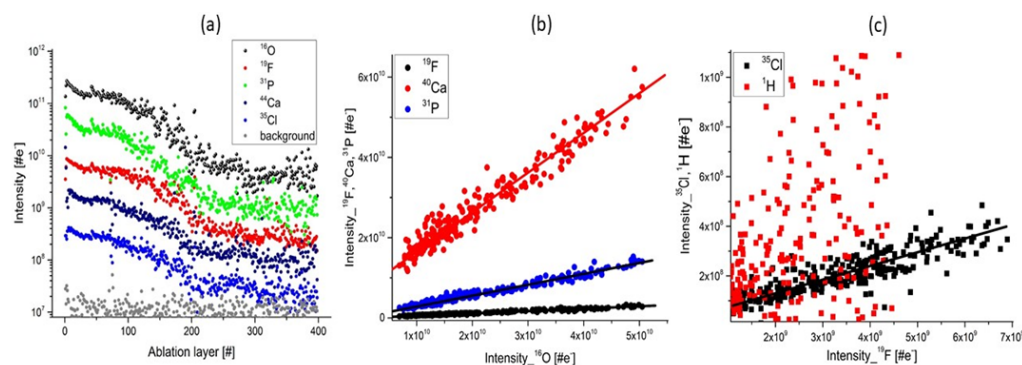


**Figure 8.** The depth profiling analysis prepared on a single ablation spot; (a) Variation of the mass peak intensities on several major elements related to apatite composition; (b) The plots of the intensity of the mass peak of Ca, P, F as function of the O intensity. The linear relationship indicates that these elements have their origin in apatite; (c) The intensity of Cl, H as function of F intensity. The linear correlation of Cl and F is observed. H and F are observed to be less correlated and the plot shows a wide distribution of data points. This is accounting for the presence of water adsorbed on the topmost sample surface.

To derive the hydrogen abundance in apatite, the (F, Cl) volatile halogen element abundances were obtained using the element intensity correlation analysis for the data set at each studied location and applying the correction coefficient for each element. The respective calibration coefficients were obtained from measurements of the geological standard (SRM 610). This method yields improved accuracy comparing with the integration method on the composed mass spectrum from one location [86]. With the (F, Cl) abundance values, the procedure used in the geological practise for determination of the OH abundance is applied. Taking XF ( $XF = CF/3.767$ , where CF is the concentration of F in apatite (wt.%) and XCl ( $XCl = CCl/6.809$ , where CCl is the concentration of Cl in apatite (wt.%) as the mole fraction of fluorapatite and chlorapatite, respectively, one can derive XH as the mole fraction of hydroxyapatite as follows:  $XH = 1 - XF - XCl$ . Inherent in these calculations is the assumption that the halogen site is filled with Cl, F and OH, only, and that the major constituents in apatite do not vary appreciably from calcium and phosphorus. The calculation may not be appropriate where considerable substitution of the Ca ion by other cations in apatite occurs. Our analysis yields values for F, Cl and OH 3.39, 0.04 and 0.09 wt.%, respectively. These results agree with former studies where the fluorine content was observed to vary between 2.02 and 3.41 wt.% with a theoretical maximum value of 3.73 wt.% for apatite from carbonatite, phoscorite and pyroxenite rocks. The reported content of Cl was typically lower than 0.09 wt.% [46,117], in agreement with our results. Considering the ratio derived in the intensity correlation of Cl and F and calibration coefficient for Cl, again an uncertainty of about 20% is expected resulting from the uncertainty of the determination of the calibration coefficients. Furthermore, the measured H concentrations, when determined from the intensity correlation method, are about five times too large. The high values from the correlation method are accounted for by contaminations of the apatite sample surface through atmospheric water. Similar investigations

can be conducted on the lunar surface. Several recent studies on lunar materials emphasize the importance of halogen components in understanding magmatic processes on the Moon. Apatite is thought to represent a record localising degassing during the final stages of the lunar magma ocean or later melt crystallisation [118], e.g., the analysis of the distribution of F, Cl, OH, including the isotope composition of Cl, can be an indicator of physical or chemical processes, such as degassing, while plasma cools down [119–127]. The volatile budget of lunar magmatic rocks can be derived this way [128]. The first apatites found in lunar samples were in the form of inclusions within minerals (pyroxferroite, fayalite, silica, ilmenite) [129–132]. Apatite also has the ability to incorporate other elements and molecular ions efficiently by substitution or adsorption onto its crystallite surface [133]. Halogens in the apatite crystal structure are used to determine the initial F and Cl concentrations of magmas and fugacity ratios [134]. In most magmatic rocks, the fluoroapatite component dominates over chlorine and hydroxylapatites [135]. Halogen abundances are important for understanding the fluid–rock interaction [136–138] and the formation of perchlorite in volcanic fumaroles [139–141].

Figure 9 displays element concentration maps for the investigated sample surface. The spatial heterogeneities of the element concentrations are readily observed both in the apatite crystal locations and outside the apatite area for several elements. Although the apatite crystal can be generally considered as highly pure, the systematic element concentration change at the trace element concentration levels can be observed and be an indicator of the environmental influence on the crystal growth (via element zoning). Microscopic intrusions are otherwise identified by the measurements of distinctly different chemical composition. Monovalent  $\text{Na}^+$ , many divalent cations ( $\text{Sr}^{2+}$ ,  $\text{Pb}^{2+}$ ,  $\text{Ba}^{2+}$ ,  $\text{Mn}^{2+}$ , etc.), trivalent ( $\text{REE}^{3+}$ ) and tetravalent cations ( $\text{Th}^{4+}$ ,  $\text{U}^{4+}$ ) are known to substitute for Ca in the apatite-group leading to a Ca deficiency in the apatite crystal. The phosphate ion  $(\text{PO}_4)^{3-}$  is commonly replaced by a variety of tetrahedral anion groups [ $(\text{MnO}_4)^{3-}$ ,  $(\text{SO}_4)^{3-}$ ,  $(\text{SiO}_4)^{3-}$ , and  $(\text{CO}_3)^{3-}$ ]. The uptake of REEs in natural apatite is highest in the range of Nd–Gd. An increase in  $\text{SiO}_2$  content in the melt is expected to promote the coupled substitution:  $(\text{REE})^{3+} + (\text{SiO}_4)^{4-} = \text{Ca}^{2+} + (\text{PO}_4)^{3-}$ , known as the britholite substitution reaction [46]. Figure 8 displays the Ca, P, O and F concentration distributions and the concentrations of main elements referenced to the oxygen concentration. There are no significant differences in concentration across the analysed surface upper right and lower left corners. At the upper right corner of the investigated area (see Figure 7), a change in chemical composition from the apatite mineral to another mineralogical phase via a rim transition is observed, whereas in the bottom left corner the presence of an inclusion of distinctly different composition is noted. Further, the Na, Mg and Si element concentrations are observed to decrease from the right to left side of the sample area, indicating the differences in the substitution rate of these elements as the crystal grew. At the rim the abundance of O decreases but no significant increase in the other elements can be seen. In some of the locations, the Sr concentrations are observed to undergo an oscillatory-like fashion and the concentrations of the elements Ce and La are observed to decrease in the direction from the crystal core to the rim. Behind the rim the intensities of La, Ba and Mg increase significantly. Similar correlations are observed in a few locations in the bottom left corner. The presence of a mineral other than apatite or the possible increase in element exchange within the apatite structure by substitution at Ca and P sites with F, Si, Sr, Mn, La, Ce can be determined from the element abundance ratios or distinct element concentration decrease [142–146]. The chemical maps data indicate that the heterogeneities occur rather systematically than randomly.

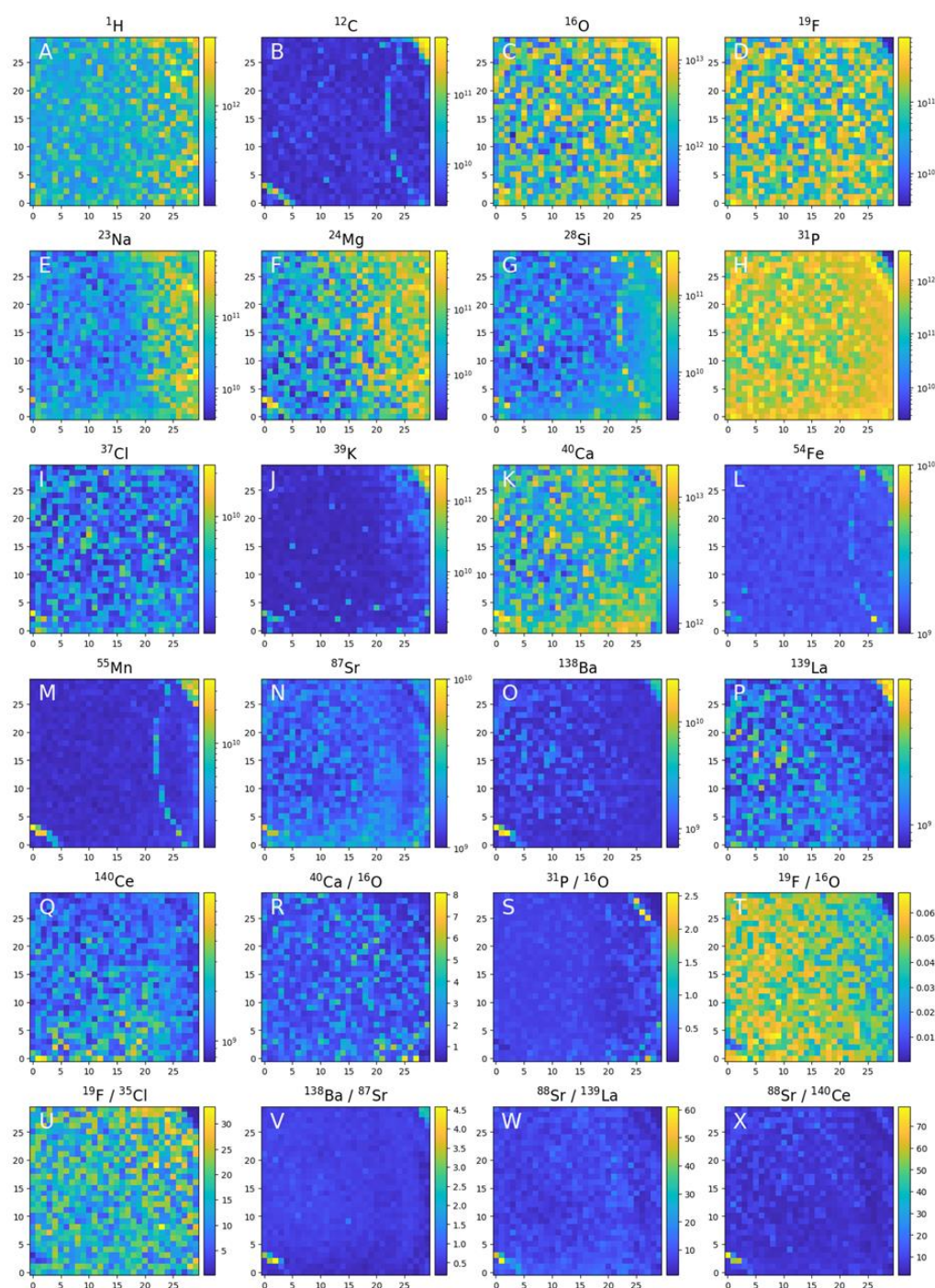


**Figure 9.** Chemical mapping of the  $0.9 \times 0.9 \text{ mm}^2$  of the apatite crystal surface embedded in phosphorite rock. Element heterogeneities measured in 900 locations can be used to investigate element analysis, analysis of the neighbouring mineral phases and identification of grain size inclusion of distinct chemical composition with assessing their mineralogical content.

Variation of the trace elements, e.g., Na, Mg, Cl in the melt or fluid usually affects the uptake of REEs by apatite because they participate directly in coupled substitutions for the incorporation of REEs [147]. The observation of systematic variations in the F, Cl, H relative concentration ratios in apatite typically reflects the change of chemical equilibrium with temperature. Their analysis is helpful in understanding magmatic differentiation [134,148], as well as hydrothermal differentiation and can be used to determine volatile fractions at the planet formation phase [149–151]. The Sr, REE, Ba ions, measured in apatite crystal

can be taken from the surrounding environment and fluids if present [142–144]. This capability allows us to analyse primary geological processes and a wide range of material transformations, including relevant timescales and rates. REE-rich mineral crystallisation influences REE content of residual magma and, together with the content of Sr in apatite, can yield the clue to crystallisation phases [145]. Observations of chemically zoned apatite via Cl, O, Sr and REE have been reported in several studies using SIMS, LA-ICPMS and optical analytical techniques [46,117,152,153]. This study is the first to report such measurements by laser ablation/ionisation mass spectrometry.

In our studies, we also observe an enhancement in abundances of several other elements (including Fe, Na, K, Ca, Mn and Si) in various locations. Calcite phase was identified behind the rim (see also right side, upper corner in Figure 7). Moreover, calcite intrusions are consistent with the presence of magnetite ( $\text{Fe}^{2+}\text{Fe}^{3+}_2\text{O}_4$ ), olivine ( $\text{MSiO}_4$ , where M = Ca, Fe, Mn, Ni, Mg), and are associated with carbonatites, e.g., dolomite  $\text{CaMg}(\text{CO}_3)_2$ , calcite  $\text{CaCO}_3$ , gregoryite  $(\text{Na,K})_2\text{CaCO}_3$ , ankerite,  $\text{Ca}(\text{Fe}^{2+},\text{Mg})(\text{CO}_3)_2$ , nyerereite  $\text{Na}_2\text{Ca}(\text{CO}_3)_2$ , or siderite  $\text{FeCO}_3$ . This observation is consistent with the results of other analyses of Phalaborwa rocks [154,155]. The ternary elemental correlation, combined with other techniques, such as Raman and IR spectroscopic analysis, would give more detailed mineralogical classification when applied in in-situ investigations [80]. The current performance of our miniature LIMS instrument to study in-situ the chemical composition of apatite is sufficiently high to measure volatiles and nearly all relevant (F, P, Cl, Ca, Sr) trace elements, including REE, which allows for a systematic quantitative analysis of their distribution. The analysis of volatiles and elemental zoning in-situ will be important to investigate magmatic planetary transformations.

## 5. Summary and Outlook

Progress in understanding the chemical composition of planetary bodies has been achieved so far by remote instruments aboard rovers, landers and orbiting spacecrafts. The results obtained by the spectroscopic, mineralogical and geochemical techniques used to analyse the surfaces of planets and their moons, asteroids and comets combined with the information extraction/processing techniques enable a range of planetary geological processes to be tracked, as well as the understanding of the composition of the planetary surface. Although continuing improvements of the space instrumentation allow for higher spatially resolved analysis, high spectral resolution and increased spectral range, the introduction of new space analytical technologies based on mass spectrometric analysis of planetary rocks and soils is required, which allows for achieving increasingly higher detection sensitivity, trace element and isotope compositional measurements.

The LMS instrument and the results conducted on several meteoritic and minerals samples demonstrate that laser-based mass spectrometric technologies are one of the most promising instruments for delivering high spatial (lateral and vertical) resolution down to micrometre or sub-micrometre level. Thus, the in-situ studies of spatial heterogeneities of elements at the trace element level can be conducted systematically allowing detailed analysis of modal mineralogy and elemental zoning in case of mineralogical grains and crystals. The analysis of trace elements and their isotopes are a powerful tool for understanding geological processes, which led to material formation and transformation. The LMS analysis at the grain of sedimentary rocks demonstrates that the instrument can be applied for searches of past and present micrometre-sized life forms. The measurements of biologically relevant element and isotope fractionation effects and the characterisation of the surrounding mineralogical phases yield information on important biosignatures and conditions for the habitability of the investigated locality.

**Author Contributions:** Conceptualization, M.T.; writing—original draft preparation, M.T.; writing—review and editing, all authors; supervision, P.W.; project administration, P.W.; funding acquisition, P.W. All authors have read and agreed to the published version of the manuscript.

**Funding:** This research was funded by the Swiss National Science Foundation (grant 200020\_184657), the NCCR PlanetS (grant 51NF40-182901) and Swiss National Science Foundation Ambizione grant (grant PZ00P2\_193453).

**Data Availability Statement:** Not applicable.

**Acknowledgments:** The financial support by the Swiss National Science Foundation (grant 200020\_184657), the NCCR PlanetS (grant 51NF40-182901) and Swiss National Science Foundation Ambizione grant (grant PZ00P2\_193453) are gratefully acknowledged.

**Conflicts of Interest:** The authors declare no conflict of interest.

## References

1. MacPherson, G.J.; Thiemens, M.H. Cosmochemistry: Understanding the solar system through analysis of extraterrestrial materials. *Proc. Natl. Acad. Sci. USA* **2011**, *108*, 19130–19134. [[CrossRef](#)] [[PubMed](#)]
2. Bishop, J.L.; Bell, J.F.L.; Moersch, J.E. *Remote Compositional Analysis: Techniques for Understanding Spectroscopy, Mineralogy, and Geochemistry of Planetary Surfaces*; Cambridge University Press: Cambridge, UK, 2022. [[CrossRef](#)]
3. Pieters, C.M.; Englert, P.A.J. *Remote Geochemical Analysis: Elemental and Mineralogical Composition*; Cambridge University Press: Cambridge, UK, 1993; Volume 4.
4. Kim, K.J.; Hasebe, N. Nuclear Planetology: Especially Concerning the Moon and Mars. *Res. Astron. Astrophys.* **2012**, *12*, 1313–1380. [[CrossRef](#)]
5. Prettyman, T.H. Remote chemical sensing using nuclear spectroscopy. In *Encyclopedia of the Solar System*; Academic Press: New York, NY, USA, 2006; Volume 2, pp. 765–786.
6. Ashley, J.W.; Golombek, M.P.; Christensen, P.R.; Squyres, S.W.; McCoy, T.J.; Schroder, C.; Fleischer, I.; Johnson, J.R.; Herkenhoff, K.E.; Parker, T.J. Evidence for mechanical and chemical alteration of iron-nickel meteorites on Mars: Process insights for Meridiani Planum. *J. Geophys. Res.-Planet* **2011**, *116*, E00f20. [[CrossRef](#)]
7. Adler, I.; Trombka, J.I.; Gorenste, P. Remote Chemical-Analysis during Apollo-15 Mission. *Anal. Chem.* **1972**, *44*, A28. [[CrossRef](#)]
8. Adler, I.; Trombka, J.I. Orbital Chemistry—Lunar-Surface Analysis from X-Ray and Gamma-Ray Remote-Sensing Experiments. *Phys. Chem. Earth* **1977**, *10*, 17–43. [[CrossRef](#)]
9. Grande, M.; Browning, R.; Waltham, N.; Parker, D.; Dunkin, S.K.; Kent, B.; Kellett, B.; Perry, C.H.; Swinyard, B.; Perry, A.; et al. The D-CIXS X-ray mapping spectrometer on SMART-1. *Planet Space Sci.* **2003**, *51*, 427–433. [[CrossRef](#)]
10. Foing, B.H.; Racca, G.D.; Marini, A.; Heather, D.J.; Koschny, D.; Grande, M.; Huovelin, J.; Keller, H.U.; Nathues, A.; Josset, J.L.; et al. SMART-1 mission to the moon: Technology and science goals. *Adv. Space Res.* **2003**, *31*, 2323–2333. [[CrossRef](#)]
11. Sun, H.X.; Dai, S.W. Mission objectives and payloads for the first lunar exploration of China. *Acta Astronaut.* **2005**, *57*, 561–565. [[CrossRef](#)]
12. Shirai, K.; Okada, T.; Yamamoto, Y.; Arai, T.; Ogawa, K.; Shiraiishi, H.; Iwasaki, M.; Arakawa, M.; Grande, M.; Kato, M. Instrumentation and performance evaluation of the XRS on SELENE orbiter. *Earth Planets Space* **2008**, *60*, 277–281. [[CrossRef](#)]
13. Karouji, Y.; Hasebe, N.; Shibamura, E.; Kobayashi, M.N.; Okudaira, O.; Yamashita, N.; Kobayashi, S.; Hareyama, M.; Miyachi, T.; Kodaira, S.; et al. Elemental mapping of the moon by the selene GRS observation. *Meteorit. Planet. Sci.* **2008**, *43*, A70.
14. Grande, M.; Maddison, B.J.; Howe, C.J.; Kellett, B.J.; Sreekumar, P.; Huovelin, J.; Crawford, I.A.; Duston, C.L.; Smith, D.; Anand, M.; et al. The C1XS X-ray Spectrometer on Chandrayaan-1. *Planet Space Sci.* **2009**, *57*, 717–724. [[CrossRef](#)]
15. Trombka, J.I.; Nittler, L.R.; Starr, R.D.; Evans, L.G.; McCoy, T.J.; Boynton, W.V.; Burbine, T.H.; Bruckner, J.; Gorenstein, P.; Squyres, S.W.; et al. The NEAR-Shoemaker x-ray/gamma-ray spectrometer experiment: Overview and lessons learned. *Meteorit. Planet. Sci.* **2001**, *36*, 1605–1616. [[CrossRef](#)]
16. Evans, L.G.; Starr, R.D.; Bruckner, J.; Reedy, R.C.; Boynton, W.V.; Trombka, J.I.; Goldstein, J.O.; Masarik, J.; Nittler, L.R.; McCoy, T.J. Elemental composition from gamma-ray spectroscopy of the NEAR-Shoemaker landing site on 433 Eros. *Meteorit. Planet. Sci.* **2001**, *36*, 1639–1660. [[CrossRef](#)]
17. McClanahan, T.P.; Trombka, J.I.; Nittler, L.R.; Boynton, W.V.; Bruckner, J.; Squyres, S.W.; Evans, L.G.; Bhangoo, J.S.; Clark, P.E.; Floyd, S.R.; et al. Spectral analysis and compositing techniques for the Near Earth Asteroid Rendezvous (NEAR Shoemaker), X-ray and Gamma-Ray Spectrometers (XGRS). *Nucl. Instrum. Methods A* **2001**, *471*, 179–183. [[CrossRef](#)]
18. Yano, H.; Kubota, T.; Miyamoto, H.; Okada, T.; Scheeres, D.; Takagi, Y.; Yoshida, K.; Abe, M.; Abe, S.; Barnouin-Jha, O.; et al. Touchdown of the Hayabusa spacecraft at the Muses Sea on Itokawa. *Science* **2006**, *312*, 1350–1353. [[CrossRef](#)] [[PubMed](#)]
19. Russell, C.T.; Capaccioni, F.; Coradini, A.; Christensen, U.; De Sanctis, M.C.; Feldman, W.C.; Jaumann, R.; Keller, H.U.; Konopliv, A.; McCord, T.B.; et al. Dawn discovery mission to vesta and ceres: Present status. *Adv. Space Res.* **2006**, *38*, 2043–2048. [[CrossRef](#)]
20. Saunders, R.S.; Arvidson, R.E.; Badhwar, G.D.; Boynton, W.V.; Christensen, P.R.; Cucinotta, F.A.; Feldman, W.C.; Gibbs, R.G.; Kloss, C.; Landano, M.R.; et al. 2001 Mars Odyssey mission summary. *Space Sci. Rev.* **2004**, *110*, 1–36. [[CrossRef](#)]
21. Rhodes, E.A.; Evans, L.G.; Nittler, L.R.; Starr, R.D.; Sprague, A.L.; Lawrence, D.J.; McCoy, T.J.; Stockstill-Cahill, K.R.; Goldsten, J.O.; Peplowski, P.N.; et al. Analysis of MESSENGER Gamma-Ray Spectrometer data from the Mercury flybys. *Planet Space Sci.* **2011**, *59*, 1829–1841. [[CrossRef](#)]

22. Peplowski, P.N.; Blewett, D.T.; Denevi, B.W.; Evans, L.G.; Lawrence, D.J.; Nittler, L.R.; Rhodes, E.A.; Selby, C.M.; Solomon, S.C. Mapping iron abundances on the surface of Mercury: Predicted spatial resolution of the MESSENGER Gamma-Ray Spectrometer. *Planet Space Sci.* **2011**, *59*, 1654–1658. [[CrossRef](#)]
23. Peplowski, P.N.; Hamara, D.K.; Lawrence, D.J.; McCoy, T.J.; Boynton, W.V.; Evans, L.G.; Rhodes, E.A.; Solomon, S.C.; Nittler, L.R.; Sprague, A.L. Abundances of Radioactive Elements on the Surface of Mercury: First Results from the Messenger Gamma-Ray Spectrometer. *Meteorit. Planet. Sci.* **2011**, *46*, A185.
24. Patterson, J.H.; Franzgrote, E.J.; Turkevich, A.L.; Anderson, W.A.; Economou, T.E.; Griffin, H.E.; Grotch, S.L.; Sowinski, K.P. Alpha-Scattering Experiment on Surveyor 7—Comparison with Surveyors 5 and 6. *J. Geophys. Res.* **1969**, *74*, 6120. [[CrossRef](#)]
25. Turkevich, A.L.; Franzgrote, E.J.; Patterson, J.H. Chemical Composition of Lunar Surface in Mare Tranquillitatis. *Science* **1969**, *165*, 277. [[CrossRef](#)] [[PubMed](#)]
26. Clark, B.C.; Baird, A.K.; Rose, H.J.; Toulmin, P.; Christian, R.P.; Kelliher, W.C.; Castro, A.J.; Rowe, C.D.; Keil, K.; Huss, G.R. Viking X-ray-Fluorescence Experiment—Analytical Methods and Early Results. *J. Geophys. Res.* **1977**, *82*, 4577–4594. [[CrossRef](#)]
27. Rieder, R.; Economou, T.; Wanke, H.; Turkevich, A.; Crisp, J.; Bruckner, J.; Dreibus, G.; McSween, H.Y. The chemical composition of Martian soil and rocks returned by the mobile alpha proton x-ray spectrometer: Preliminary results from the x-ray mode. *Science* **1997**, *278*, 1771–1774. [[CrossRef](#)] [[PubMed](#)]
28. Gellert, R.; Rieder, R.; Bruckner, J.; Clark, B.C.; Dreibus, G.; Klingelhofer, G.; Lugmair, G.; Ming, D.W.; Wanke, H.; Yen, A.; et al. Alpha particle X-ray spectrometer (APXS): Results from Gusev crater and calibration report. *J. Geophys. Res.-Planet* **2006**, *111*, E02s05. [[CrossRef](#)]
29. Maurice, S.; Wiens, R.C.; Saccoccio, M.; Barraclough, B.; Gasnault, O.; Forni, O.; Mangold, N.; Baratoux, D.; Bender, S.; Berger, G.; et al. The ChemCam Instrument Suite on the Mars Science Laboratory (MSL) Rover: Science Objectives and Mast Unit Description. *Space Sci. Rev.* **2012**, *170*, 95–166. [[CrossRef](#)]
30. Ollila, A.M.; Newsom, H.E.; Clark, B.; Wiens, R.C.; Cousin, A.; Blank, J.G.; Mangold, N.; Sautter, V.; Maurice, S.; Clegg, S.M.; et al. Trace element geochemistry (Li, Ba, Sr, and Rb) using Curiosity's ChemCam: Early results for Gale crater from Bradbury Landing Site to Rocknest. *J. Geophys. Res.-Planet* **2014**, *119*, 255–285. [[CrossRef](#)]
31. Payre, V.; Fabre, C.; Cousin, A.; Sautter, V.; Wiens, R.C.; Forni, O.; Gasnault, O.; Mangold, N.; Meslin, P.Y.; Lasue, J.; et al. Alkali trace elements in Gale crater, Mars, with ChemCam: Calibration update and geological implications. *J. Geophys. Res.-Planet* **2017**, *122*, 650–679. [[CrossRef](#)]
32. Mccord, T.B.; Johnson, T.V.; Adams, J.B. Asteroid Vesta—Spectral Reflectivity and Compositional Implications. *Science* **1970**, *168*, 1445–1447. [[CrossRef](#)]
33. Demeo, F.E.; Binzel, R.P.; Slivan, S.M.; Bus, S.J. An extension of the Bus asteroid taxonomy into the near-infrared. *Icarus* **2009**, *202*, 160–180. [[CrossRef](#)]
34. Mustard, J.F.; Cooper, C.D. Joint analysis of ISM and TES spectra: The utility of multiple wavelength regimes for Martian surface studies. *J. Geophys. Res.-Planet* **2005**, *110*, E05012. [[CrossRef](#)]
35. Pan, L.; Ehlmann, B.L. Phyllosilicate and hydrated silica detections in the knobby terrains of Acidalia Planitia, northern plains, Mars. *Geophys. Res. Lett.* **2014**, *41*, 1890–1898. [[CrossRef](#)]
36. Morris, R.V.; Klingelhofer, G.; Schroder, C.; Fleischer, I.; Ming, D.W.; Yen, A.S.; Gellert, R.; Arvidson, R.E.; Rodionov, D.S.; Crumpler, L.S.; et al. Iron mineralogy and aqueous alteration from Husband Hill through Home Plate at Gusev Crater, Mars: Results from the Mossbauer instrument on the Spirit Mars Exploration Rover. *J. Geophys. Res.-Planet* **2008**, *113*, E12s42. [[CrossRef](#)]
37. Snyder, G.A.; Taylor, L.A.; Neal, C.R. A chemical model for generating the sources of mare basalts-combined equilibrium and fractional crystallisation of the lunar magmasphere. *Geochim. Cosmochim. Acta* **1992**, *56*, 3809–3823. [[CrossRef](#)]
38. Le Corre, L.; Reddy, V.; Schmedemann, N.; Becker, K.J.; O'Brien, D.P.; Yamashita, N.; Peplowski, P.N.; Prettyman, T.H.; Li, J.Y.; Cloutis, E.A.; et al. Olivine or impact melt: Nature of the "Orange" material on Vesta from Dawn. *Icarus* **2013**, *226*, 1568–1594. [[CrossRef](#)]
39. Shearer, C.K.; Papike, J.J.; Spilde, M.N. Trace-element partitioning between immiscible lunar melts: An example from naturally occurring lunar melt inclusions. *Am. Mineral.* **2001**, *86*, 238–246. [[CrossRef](#)]
40. Milliken, R.E.; Fischer, W.W.; Hurowitz, J.A. Missing salts on early Mars. *Geophys. Res. Lett.* **2009**, *36*, L11202. [[CrossRef](#)]
41. Schroder, S.; Pavlov, S.G.; Rauschenbach, I.; Jessberger, E.K.; Hubers, H.W. Detection and identification of salts and frozen salt solutions combining laser-induced breakdown spectroscopy and multivariate analysis methods: A study for future martian exploration. *Icarus* **2013**, *223*, 61–73. [[CrossRef](#)]
42. Meslin, P.Y.; Gasnault, O.; Forni, O.; Schroder, S.; Cousin, A.; Berger, G.; Clegg, S.M.; Lasue, J.; Maurice, S.; Sautter, V.; et al. Soil Diversity and Hydration as Observed by ChemCam at Gale Crater, Mars. *Science* **2013**, *341*, 1238670. [[CrossRef](#)]
43. Grotzinger, J.P.; Crisp, J.; Vasavada, A.R.; Anderson, R.C.; Baker, C.J.; Barry, R.; Blake, D.F.; Conrad, P.; Edgett, K.S.; Ferdowski, B.; et al. Mars Science Laboratory Mission and Science Investigation. *Space Sci. Rev.* **2012**, *170*, 5–56. [[CrossRef](#)]
44. National Academies of Sciences, Engineering, and Medicine. *Origins, Worlds, and Life: A Decadal Strategy for Planetary Science and Astrobiology 2023–2032 (2022)*; The National Academies Press: Washington, DC, USA, 2022. [[CrossRef](#)]
45. Putirka, K.D. (Ed.) *Introduction to Minerals, Inclusions and Volcanic Processes*; Walter de Gruyter GmbH & Co KG: Berlin, Germany, 2008; Volume 69, pp. 1–8.

46. Milani, L.; Bolhar, R.; Frei, D.; Harlov, D.E.; Samuel, V.O. Light rare earth element systematics as a tool for investigating the petrogenesis of phoscorite-carbonatite associations, as exemplified by the Phalaborwa Complex, South Africa. *Miner. Depos.* **2017**, *52*, 1105–1125. [[CrossRef](#)]
47. Peplowski, P.N.; Klima, R.L.; Lawrence, D.J.; Ernst, C.M.; Denevi, B.W.; Frank, E.A.; Goldsten, J.O.; Murchie, S.L.; Nittler, L.R.; Solomon, S.C. Remote sensing evidence for an ancient carbon-bearing crust on Mercury. *Nat. Geosci.* **2016**, *9*, 273. [[CrossRef](#)]
48. Watson, E.B. Apatite and Phosphorus in Mantle Source Regions—An Experimental-Study of Apatite-Melt Equilibria at Pressures to 25-Kbar. *Earth Planet. Sci. Lett.* **1980**, *51*, 322–335. [[CrossRef](#)]
49. Rubatto, D. Zircon: The Metamorphic Mineral. *Petrochronol. Methods Appl.* **2017**, *83*, 261–295. [[CrossRef](#)]
50. Arevalo, R.; Selliez, L.; Briois, C.; Carrasco, N.; Thirkell, L.; Cherville, B.; Colin, F.; Gaubicher, B.; Farcy, B.; Li, X.; et al. An Orbitrap-based laser desorption/ablation mass spectrometer designed for spaceflight. *Rapid Commun. Mass Spectrom.* **2018**, *32*, 1875–1886. [[CrossRef](#)]
51. Willhite, L.; Ni, Z.Q.; Arevalo, R.; Bardyn, A.; Gundersen, C.; Minasola, N.; Southard, A.; Briois, C.; Thirkell, L.; Colin, F.; et al. CORALS: A Laser Desorption/Ablation Orbitrap Mass Spectrometer for In Situ Exploration of Europa. *Aerosp. Conf. Proc.* **2021**, 1–13. [[CrossRef](#)]
52. Briois, C.; Thissen, R.; Thirkell, L.; Aradj, K.; Bouabdellah, A.; Boukrara, A.; Carrasco, N.; Chalumeau, G.; Chapelon, O.; Colin, F.; et al. Orbitrap mass analyser for in situ characterisation of planetary environments: Performance evaluation of a laboratory prototype. *Planet Space Sci.* **2016**, *131*, 33–45. [[CrossRef](#)]
53. Arevalo, R.; Ni, Z.Q.; Danell, R.M. Mass spectrometry and planetary exploration: A brief review and future projection. *J. Mass Spectrom.* **2020**, *55*, e4454. [[CrossRef](#)]
54. Brinckerhoff, W.B.; Managadze, G.G.; McEntire, R.W.; Cheng, A.F.; Green, W.J. Laser time-of-flight mass spectrometry for space. *Rev. Sci. Instrum.* **2000**, *71*, 536–545. [[CrossRef](#)]
55. Managadze, G.G.; Wurz, P.; Sagdeev, R.Z.; Chumikov, A.E.; Tulej, M.; Yakovleva, M.; Managadze, N.G.; Bondarenko, A.L. Study of the main geochemical characteristics of Phobos' regolith using laser time-of-flight mass spectrometry. *Solar Syst. Res.* **2010**, *44*, 376–384. [[CrossRef](#)]
56. Rohner, U.; Whitby, J.A.; Wurz, P. A miniature laser ablation time-of-flight mass spectrometer for in situ planetary exploration. *Meas. Sci. Technol.* **2003**, *14*, 2159–2164. [[CrossRef](#)]
57. Riedo, A.; Bieler, A.; Neuland, M.; Tulej, M.; Wurz, P. Performance evaluation of a miniature laser ablation time-of-flight mass spectrometer designed for in situ investigations in planetary space research. *J. Mass Spectrom.* **2013**, *48*, 1–15. [[CrossRef](#)] [[PubMed](#)]
58. Tulej, M.; Riedo, A.; Neuland, M.B.; Meyer, S.; Wurz, P.; Thomas, N.; Grimaudo, V.; Moreno-Garcia, P.; Broekmann, P.; Neubeck, A.; et al. CAMAM: A Miniature Laser Ablation Ionisation Mass Spectrometer and Microscope-Camera System for In Situ Investigation of the Composition and Morphology of Extraterrestrial Materials. *Geostand. Geoanal. Res.* **2014**, *38*, 441–466. [[CrossRef](#)]
59. Sinha, M.P.; Wadsworth, M. Miniature focal plane mass spectrometer with 1000-pixel modified-CCD detector array for direct ion measurement. *Rev. Sci. Instrum.* **2005**, *76*, 025103. [[CrossRef](#)]
60. Cohen, B.A.; Miller, J.S.; Li, Z.H.; Swindle, T.D.; French, R.A. The Potassium-Argon Laser Experiment (KArLE): In Situ Geochronology for Planetary Robotic Missions. *Geostand. Geoanal. Res.* **2014**, *38*, 421–439. [[CrossRef](#)]
61. Cho, Y.; Cohen, B.A. Dating igneous rocks using the Potassium-Argon Laser Experiment (KArLE) instrument: A case study for similar to 380Ma basaltic rocks. *Rapid Commun. Mass Spectrom.* **2018**, *32*, 1755–1765. [[CrossRef](#)]
62. Anderson, F.S.; Nowicki, K.; Whitaker, T.; Mahoney, J.; Young, D.; Miller, G.; Waite, H.; Norman, M.; Boyce, J.; Taylor, J. A Laser Desorption Resonance Ionization Mass Spectrometer for Rb-Sr Geochronology: Sr Isotope Results. In Proceedings of the 2012 Ieee Aerospace Conference, Big Sky, MT, USA, 3–10 March 2012.
63. Anderson, F.S.; Levine, J.; Whitaker, T. Dating a Martian meteorite with 20 Myr precision using a prototype in-situ dating instrument. *Planet Space Sci.* **2020**, *191*, 105007. [[CrossRef](#)]
64. Balaram, V.; Sawant, S.S. Indicator Minerals, Pathfinder Elements, and Portable Analytical Instruments in Mineral Exploration Studies. *Minerals* **2022**, *12*, 394. [[CrossRef](#)]
65. Balaram, V. Current Advances in Miniaturization of Analytical Instruments—Applications in Cosmochemistry, Geochemistry, Exploration and Environmental Sciences. *Spectroscopy* **2016**, *31*, 40–44.
66. Hornung, K.; Kissel, J.; Fischer, H.; Mellado, E.M.; Kulikov, O.; Hilchenbach, M.; Kruger, H.; Engrand, C.; Langevin, Y.; Rossi, M.; et al. Collecting cometary dust particles on metal blacks with the COSIMA instrument onboard ROSETTA. *Planet Space Sci.* **2014**, *103*, 309–317. [[CrossRef](#)]
67. Franzke, J.; Miclea, M. Sample analysis with miniaturized plasmas. *Appl. Spectrosc.* **2006**, *60*, 80a–90a. [[CrossRef](#)] [[PubMed](#)]
68. Franzke, J.; Kunze, K.; Miclea, M.; Niemax, K. Microplasmas for analytical spectrometry. *J. Anal. Atom. Spectrom.* **2003**, *18*, 802–807. [[CrossRef](#)]
69. Farcy, B.J.; Arevalo, R.D.; Taghioskoui, M.; McDonough, W.F.; Benna, M.; Brinckerhoff, W.B. A prospective microwave plasma source for in situ spaceflight applications. *J. Anal. Atom. Spectrom.* **2020**, *35*, 2740–2747. [[CrossRef](#)]
70. Tulej, M.; Wiesendanger, R.; Riedo, A.; Knopp, G.; Wurz, P. Mass spectrometric analysis of the Mg plasma produced by double-pulse femtosecond laser irradiation. *J. Anal. Atom. Spectrom.* **2018**, *33*, 1292–1303. [[CrossRef](#)]
71. Wiesendanger, R.; Tulej, M.; Riedo, A.; Frey, S.; Shea, H.; Wurz, P. Improved detection sensitivity for heavy trace elements using a miniature laser ablation ionisation mass spectrometer. *J. Anal. Atom. Spectrom.* **2017**, *32*, 2182–2188. [[CrossRef](#)]

72. Riedo, A.; Grimaudo, V.; Lopez, A.C.; Tulej, M.; Wurz, P.; Broekmann, P. Novel 2D binning approach for advanced LIMS depth profiling analysis. *J. Anal. Atom. Spectrom.* **2019**, *34*, 1564–1570. [[CrossRef](#)]
73. Riedo, A.; Lukmanov, R.; Grimaudo, V.; Koning, C.; Ligterink, N.F.W.; Tulej, M.; Wurz, P. Improved plasma stoichiometry recorded by laser ablation ionization mass spectrometry using a double-pulse femtosecond laser ablation ion source. *Rapid Commun. Mass Spectrom.* **2021**, *35*, e9094. [[CrossRef](#)]
74. Neuland, M.B.; Meyer, S.; Mezger, K.; Riedo, A.; Tulej, M.; Wurz, P. Probing the Allende meteorite with a miniature laser-ablation mass analyser for space application. *Planet Space Sci.* **2014**, *101*, 196–209. [[CrossRef](#)]
75. Frey, S.; Wiesendanger, R.; Tulej, M.; Neuland, M.; Riedo, A.; Grimaudo, V.; Moreno-Garcia, P.; Lopez, A.C.; Mohos, M.; Hofmann, B.; et al. Chemical analysis of a lunar meteorite by laser ablation mass spectrometry. *Planet Space Sci.* **2020**, *182*, 104816. [[CrossRef](#)]
76. Grimaudo, V.; Moreno-Garcia, P.; Lopez, A.C.; Riedo, A.; Wiesendanger, R.; Tulej, M.; Gruber, C.; Lortscher, E.; Wurz, P.; Broekmann, P. Depth Profiling and Cross-Sectional Laser Ablation Ionization Mass Spectrometry Studies of Through-Silicon-Vias. *Anal. Chem.* **2018**, *90*, 5179–5186. [[CrossRef](#)]
77. Grimaudo, V.; Moreno-Garcia, P.; Riedo, A.; Meyer, S.; Tulej, M.; Neuland, M.B.; Mohos, M.; Gutz, C.; Waldvoegek, S.R.; Wurz, P.; et al. Toward Three-Dimensional Chemical Imaging of Ternary Cu-Sn-Pb Alloys Using Femtosecond Laser Ablation/Ionization Mass Spectrometry. *Anal. Chem.* **2017**, *89*, 1632–1641. [[CrossRef](#)]
78. Grimaudo, V.; Moreno-Garcia, P.; Riedo, A.; Neuland, M.B.; Tulej, M.; Broekmann, P.; Wurz, P. High-Resolution Chemical Depth Profiling of Solid Material Using a Miniature Laser Ablation/Ionization Mass Spectrometer. *Anal. Chem.* **2015**, *87*, 2037–2041. [[CrossRef](#)] [[PubMed](#)]
79. Grimaudo, V.; Tulej, M.; Riedo, A.; Lukmanov, R.; Ligterink, N.F.W.; de Koning, C.; Wurz, P. UV post-ionization laser ablation ionization mass spectrometry for improved nm-depth profiling resolution on Cr/Ni reference standard. *Rapid Commun. Mass Spectrom.* **2020**, *34*, e8803. [[CrossRef](#)] [[PubMed](#)]
80. Neubeck, A.; Tulej, M.; Ivarsson, M.; Broman, C.; Riedo, A.; McMahon, S.; Wurz, P.; Bengtson, S. Mineralogical determination in situ of a highly heterogeneous material using a miniaturized laser ablation mass spectrometer with high spatial resolution. *Int. J. Astrobiol.* **2016**, *15*, 133–146. [[CrossRef](#)]
81. Tulej, M.; Lukmanov, R.; Grimaudo, V.; Riedo, A.; de Koning, C.; Ligterink, N.; Neubeck, A.; Ivarsson, M.; McMahon, S.; Wurz, P. Determination of microscopic mineralogy of inclusion in an amygdaloidal pillow basalt by fs-LIMS. *J. Anal. At. Spectrom.* **2021**, *36*, 80–91. [[CrossRef](#)]
82. Riedo, A.; de Koning, C.; Stevens, A.H.; Cockell, C.S.; McDonald, A.; Lopez, A.C.; Grimaudo, V.; Tulej, M.; Wurz, P.; Ehrenfreund, P. The Detection of Elemental Signatures of Microbes in Martian Mudstone Analogs Using High Spatial Resolution Laser Ablation Ionization Mass Spectrometry. *Astrobiology* **2020**, *20*, 1224–1235. [[CrossRef](#)]
83. Wiesendanger, R.; Wacey, D.; Tulej, M.; Neubeck, A.; Ivarsson, M.; Grimaudo, V.; Moreno-Garcia, P.; Cedeno-Lopez, A.; Riedo, A.; Wurz, P. Chemical and optical identification of micrometer-sized 1.9 billion-year-old fossils by combining a miniature laser ablation ionization mass spectrometry system with an optical microscope. *Astrobiology* **2018**, *18*, 1071–1080. [[CrossRef](#)]
84. Meyer, S.; Riedo, A.; Neuland, M.B.; Tulej, M.; Wurz, P. Fully automatic and precise data analysis developed for time-of-flight mass spectrometry. *J. Mass Spectrom.* **2017**, *52*, 580–590. [[CrossRef](#)]
85. Wiesendanger, R.A.; Tulej, M.; Grimaudo, V.; Cedeno-Lopez, A.C.; Lukmanov, R.; Riedo, A.; Wurz, P. A method for improvement of mass resolution and isotope accuracy for laser ablation time-of-flight mass spectrometers. *J. Chemometr.* **2019**, *33*, e3081. [[CrossRef](#)]
86. Tulej, M.; Neubeck, A.; Riedo, A.; Lukmanov, R.; Grimaudo, V.; Ligterink, N.F.W.; Ivarsson, M.; Bach, W.; de Koning, C.; Wurz, P. Isotope abundance ratio measurements using femtosecond laser ablation ionization mass spectrometry. *J. Mass Spectrom.* **2020**, *55*, e4660. [[CrossRef](#)]
87. Tulej, M.; Ligterink, N.F.W.; de Koning, C.; Grimaudo, V.; Lukmanov, R.; Keresztes Schmidt, P.; Riedo, A.; Wurz, P. Current Progress in Femtosecond Laser Ablation/Ionisation Time-of-Flight Mass Spectrometry. *Appl. Sci.* **2021**, *11*, 2562. [[CrossRef](#)]
88. Riedo, A.; Neuland, M.; Meyer, S.; Tulej, M.; Wurz, P. Coupling of LMS with a fs-laser ablation ion source: Elemental and isotope composition measurements. *J. Anal. Atom. Spectrom.* **2013**, *28*, 1256–1269. [[CrossRef](#)]
89. Neuland, M.B.; Grimaudo, V.; Mezger, K.; Moreno-Garcia, P.; Riedo, A.; Tulej, M.; Wurz, P. Quantitative measurement of the chemical composition of geological standards with a miniature laser ablation/ionization mass spectrometer designed for in situ application in space research. *Meas. Sci. Technol.* **2016**, *27*, 035904. [[CrossRef](#)]
90. Tulej, M.; Iakovleva, M.; Leya, I.; Wurz, P. A miniature mass analyser for in-situ elemental analysis of planetary material-performance studies. *Anal. Bioanal. Chem.* **2011**, *399*, 2185–2200. [[CrossRef](#)] [[PubMed](#)]
91. Riedo, A.; Tulej, M.; Rohner, U.; Wurz, P. High-speed microstrip multi-anode multichannel plate detector system. *Rev. Sci. Instrum.* **2017**, *88*, 045114. [[CrossRef](#)] [[PubMed](#)]
92. Riedo, A.; Meyer, S.; Heredia, B.; Neuland, M.B.; Bieler, A.; Tulej, M.; Leya, I.; Iakovleva, M.; Mezger, K.; Wurz, P. Highly accurate isotope composition measurements by a miniature laser ablation mass spectrometer designed for in situ investigations on planetary surfaces. *Planet Space Sci.* **2013**, *87*, 1–13. [[CrossRef](#)]
93. Riedo, A.; Grimaudo, V.; Aerts, J.W.; Lukmanov, R.; Tulej, M.; Broekmann, P.; Lindner, R.; Wurz, P.; Ehrenfreund, P. Laser Ablation Ionization Mass Spectrometry: A Space Prototype System for In Situ Sulphur Isotope Fractionation Analysis on Planetary Surfaces. *Front. Astron. Space* **2021**, *8*, 726373. [[CrossRef](#)]

94. Lopez, D.M.; Grimaudo, V.; Prone, G.; Flisch, A.; Riedo, A.; Zboray, R.; Luthi, T.; Mayor, M.; Fussenegger, M.; Broekmann, P.; et al. Automated, 3-D and Sub-Micron Accurate Ablation-Volume Determination by Inverse Molding and X-Ray Computed Tomography. *Adv. Sci.* **2022**, *9*, 2200136. [[CrossRef](#)]
95. Lopez, A.C.; Grimaudo, V.; Riedo, A.; Tulej, M.; Wiesendanger, R.; Lukmanov, R.; Moreno-Garcia, P.; Lortscher, E.; Wurz, P.; Broekmann, P. Three-Dimensional Composition Analysis of SnAg Solder Bumps Using Ultraviolet Femtosecond Laser Ablation Ionization Mass Spectrometry. *Anal. Chem.* **2020**, *92*, 1355–1362. [[CrossRef](#)]
96. Grimaudo, V.; Moreno-Garcia, P.; Riedo, A.; Lopez, A.C.; Tulej, M.; Wiesendanger, R.; Wurz, P.; Broekmann, P. Review-Laser Ablation Ionization Mass Spectrometry (LIMS) for Analysis of Electrodeposited Cu Interconnects. *J. Electrochem. Soc.* **2018**, *166*, D3190–D3199. [[CrossRef](#)]
97. Azov, V.A.; Mueller, L.; Makarov, A.A. Laser ionization mass spectrometry at 55: Quo Vadis? *Mass Spectrom. Rev.* **2020**, *21669*, 1–52. [[CrossRef](#)]
98. Sauer, S.; Freiwald, A.; Maier, T.; Kube, M.; Reinhardt, R.; Kostrzewa, M.; Geider, K. Classification and Identification of Bacteria by Mass Spectrometry and Computational Analysis. *PLoS ONE* **2008**, *3*, e2843. [[CrossRef](#)] [[PubMed](#)]
99. Behrmann, J.; Etmann, C.; Boskamp, T.; Casadonte, R.; Kriegsmann, J.; Maass, P. Deep learning for tumor classification in imaging mass spectrometry. *Bioinformatics* **2018**, *34*, 1215–1223. [[CrossRef](#)] [[PubMed](#)]
100. Lukmanov, R. Characterization of Bio-Organic and Inorganic Chemistries Using Laser-Based Mass Spectrometry. Ph. D. Thesis, University Bern, Bern, Switzerland, 2021.
101. Lukmanov, R.A.; Tulej, M.; Ligterink, N.F.W.; De Koning, C.; Riedo, A.; Grimaudo, V.; Neubeck, A.; Wacey, D.; Wurz, P. Chemical identification of microfossils from the 1.88-Ga Gunflint chert: Towards empirical biosignatures using laser ablation ionization mass spectrometer. *J. Chemometr.* **2021**, *35*, e3370. [[CrossRef](#)]
102. Lukmanov, R.A.; Riedo, A.; Wacey, D.; Ligterink, N.F.W.; Grimaudo, V.; Tulej, M.; de Koning, C.; Neubeck, A.; Wurz, P. On Topological Analysis of fs-LIMS Data. Implications for in Situ Planetary Mass Spectrometry. *Front. Artif. Intell.* **2021**, *4*, 668163. [[CrossRef](#)]
103. Neuland, M.B.; Mezger, K.; Riedo, A.; Tulej, M.; Wurz, P. The chemical composition and homogeneity of the Allende matrix. *Planet Space Sci.* **2021**, *204*, 105251. [[CrossRef](#)]
104. Gnos, E.; Hofmann, B.A.; Al-Kathiri, A.; Lorenzetti, S.; Villa, I.; Eugster, O.; Jull, A.J.T.; Eikenberg, J.; Spettel, B.; Krähenbühl, U. Lunar meteorite SaU 169; An extremely KREEP-rich rock In Proceedings of the 66th Annual Meteoritical Society Meeting, Munster, Germany, 28 July–1 August 2003.
105. Ferry, J.M.; Watson, E.B. New thermodynamic models and revised calibrations for the Ti-in-zircon and Zr-in-rutile thermometers. *Contrib. Mineral. Petrol.* **2007**, *154*, 429–437. [[CrossRef](#)]
106. Tulej, M.; Neubeck, A.; Ivarsson, M.; Riedo, A.; Neuland, M.B.; Meyer, S.; Wurz, P. Chemical Composition of Micrometer-Sized Filaments in an Aragonite Host by a Miniature Laser Ablation/Ionization Mass Spectrometer. *Astrobiology* **2015**, *15*, 669–682. [[CrossRef](#)]
107. Buettner, K.M.; Valentine, A.M. Bioinorganic Chemistry of Titanium. *Chem. Rev.* **2012**, *112*, 1863–1881. [[CrossRef](#)]
108. Lukmanov, R.A.; Tulej, M.; Wiesendanger, R.; Riedo, A.; Grimaudo, V.; Ligterink, N.F.W.; de Koning, C.; Neubeck, A.; Wacey, D.; Wurz, P. Multiwavelength Ablation/Ionization and Mass Spectrometric Analysis of 1.88 Ga Gunflint Chert. *Astrobiology* **2022**, *22*, 369–386. [[CrossRef](#)]
109. Allen, C.C.; Westall, F.; Schelble, R.T. Importance of a Martian Hematite Site for Astrobiology. *Astrobiology* **2001**, *1*, 111–123. [[CrossRef](#)] [[PubMed](#)]
110. Belousova, E.A.; Griffin, W.L.; O'Reilly, S.Y.; Fisher, N.I. Apatite as an indicator mineral for mineral exploration: Trace-element compositions and their relationship to host rock type. *J. Geochem. Explor.* **2002**, *76*, 45–69. [[CrossRef](#)]
111. Bergman, S.C.; Ritter, C.J.; Zamierowski, E.E.; Cothorn, C.R. Use of Zonal Centrifugation in Delineating Trace-Element Distributions in Sewage Sludges from the Dayton, Ohio, Area. *J. Environ. Qual.* **1979**, *8*, 416–422. [[CrossRef](#)]
112. Boudreau, A.E.; Mathez, E.A.; Mccallum, I.S. Halogen Geochemistry of the Stillwater and Bushveld Complexes—Evidence for Transport of the Platinum-Group Elements by Cl-Rich Fluids. *J. Petrol.* **1986**, *27*, 967–986. [[CrossRef](#)]
113. Sha, L.K.; Chappell, B.W. Apatite chemical composition, determined by electron microprobe and laser-ablation inductively coupled plasma mass spectrometry, as a probe into granite petrogenesis. *Geochim. Cosmochim. Acta* **1999**, *63*, 3861–3881. [[CrossRef](#)]
114. Wu, F.Y.; Yang, Y.H.; Li, Q.L.; Mitchell, R.H.; Dawson, J.B.; Brandl, G.; Yuhara, M. In situ determination of U-Pb ages and Sr-Nd-Hf isotopic constraints on the petrogenesis of the Phalaborwa carbonatite Complex, South Africa. *Lithos* **2011**, *127*, 309–322. [[CrossRef](#)]
115. Dawson, J.B.; Hinton, R.W. Trace-element content and partitioning in calcite, dolomite and apatite in carbonatite, Phalaborwa, South Africa. *Mineral. Mag.* **2003**, *67*, 921–930. [[CrossRef](#)]
116. Giebel, R.J.; Gauert, C.D.K.; Marks, M.A.W.; Costin, G.; Markl, G. Multi-stage formation of REE minerals in the Palabora Carbonatite Complex, South Africa. *Am. Mineral.* **2017**, *102*, 1218–1233. [[CrossRef](#)]
117. Decree, S.; Cawthorn, G.; Deloule, E.; Mercadier, J.; Frimmel, H.; Baele, J.M. Unravelling the processes controlling apatite formation in the Phalaborwa Complex (South Africa) based on combined cathodoluminescence, LA-ICPMS and in-situ O and Sr isotope analyses. *Contrib. Mineral. Petrol.* **2020**, *175*, 34. [[CrossRef](#)]
118. Gargano, A.; Sharp, Z.; Shearer, C.; Simon, J.I.; Halliday, A.; Buckley, W. The Cl isotope composition and halogen contents of Apollo-return samples. *Proc. Natl. Acad. Sci. USA* **2020**, *117*, 23418–23425. [[CrossRef](#)]

119. Liu, X.; Wei, H.Z.; Li, Y.C.; Williams-Jones, A.E.; Lu, J.J.; Jiang, S.Y.; Dong, G.; Ma, J.; Eastoe, C.J. Chlorine isotope mantle heterogeneity: Constraints from theoretical first-principles calculations. *Chem. Geol.* **2021**, *572*, 120193. [[CrossRef](#)]
120. Barnes, J.D.; Sharp, Z.D. Chlorine Isotope Geochemistry. *Non-Tradit. Stable Isot.* **2017**, *82*, 345–377. [[CrossRef](#)]
121. Tartese, R.; Anand, M.; Joy, K.H.; Franchi, I.A. H and Cl isotope systematics of apatite in brecciated lunar meteorites Northwest Africa 4472, Northwest Africa 773, Sayh al Uhaymir 169, and Kalahari 009. *Meteorit. Planet. Sci.* **2014**, *49*, 2266–2289. [[CrossRef](#)]
122. Sharp, Z.D.; Shearer, C.K.; McKeegan, K.D.; Barnes, J.D.; Wang, Y.Q. The Chlorine Isotope Composition of the Moon and Implications for an Anhydrous Mantle. *Science* **2010**, *329*, 1050–1053. [[CrossRef](#)] [[PubMed](#)]
123. Boyce, J.W.; Treiman, A.H.; Guan, Y.B.; Ma, C.; Eiler, J.M.; Gross, J.; Greenwood, J.P.; Stolper, E.M. The chlorine isotope fingerprint of the lunar magma ocean. *Sci. Adv.* **2015**, *1*, e1500380. [[CrossRef](#)]
124. Treiman, A.H.; Boyce, J.W.; Gross, J.; Guan, Y.B.; Eiler, J.M.; Stolper, E.M. Phosphate-halogen metasomatism of lunar granulite 79215: Impact-induced fractionation of volatiles and incompatible elements. *Am. Mineral.* **2014**, *99*, 1860–1870. [[CrossRef](#)]
125. Potts, N.J.; Barnes, J.J.; Tartese, R.; Franchi, I.A.; Anand, M. Chlorine isotopic compositions of apatite in Apollo 14 rocks: Evidence for widespread vapor-phase metasomatism on the lunar nearside similar to 4 billion years ago. *Geochim. Cosmochim. Acta* **2018**, *230*, 46–59. [[CrossRef](#)]
126. Wang, Y.; Hsu, W.B.; Guan, Y.B. An extremely heavy chlorine reservoir in the Moon: Insights from the apatite in lunar meteorites. *Sci. Rep.* **2019**, *9*, 5727. [[CrossRef](#)]
127. Sharp, Z.; Williams, J.; Shearer, C.; Agee, C.; McKeegan, K. The chlorine isotope composition of Martian meteorites 2. Implications for the early solar system and the formation of Mars. *Meteorit. Planet. Sci.* **2016**, *51*, 2111–2126. [[CrossRef](#)]
128. Boyce, J.W.; Liu, Y.; Rossman, G.R.; Guan, Y.B.; Eiler, J.M.; Stolper, E.M.; Taylor, L.A. Lunar apatite with terrestrial volatile abundances. *Nature* **2010**, *466*, 466–469. [[CrossRef](#)]
129. Fuchs, L.H.; Olsen, E. Composition of Metal in Type Iii Carbonaceous Chondrites and Its Relevance to Source-Assignment of Lunar Metal. *Earth Planet Sci. Lett.* **1973**, *18*, 379–384. [[CrossRef](#)]
130. Reed, G.W.; Jovanovi, S.; Fuchs, L.H. Fluorine and Other Trace Elements in Lunar Plagioclase Concentrates. *Earth Planet Sci. Lett.* **1971**, *11*, 354–358. [[CrossRef](#)]
131. Reed, G.W.; Jovanovi, S.; Fuchs, L.H. Trace Elements and Accessory Minerals in Lunar Samples. *Science* **1970**, *167*, 501–503. [[CrossRef](#)] [[PubMed](#)]
132. Fuchs, L.H. Orthopyroxene-Plagioclase Fragments in Lunar Soil from Apollo-12. *Science* **1970**, *169*, 866–868. [[CrossRef](#)] [[PubMed](#)]
133. Sommerauer, J.; Katzelehnert, K. Trapped Phosphate Melt Inclusions in Silicate-Carbonate-Hydroxyapatite from Comb-Layer Alvikites from the Kaiserstuhl Carbonatite Complex (Sw-Germany). *Contrib. Mineral. Petrol.* **1985**, *91*, 354–359. [[CrossRef](#)]
134. Piccoli, P.; Candela, P. Apatite in Felsic Rocks—A Model for the Estimation of Initial Halogen Concentrations in the Bishop Tuff (Long Valley) and Tuolumne Intrusive Suite (Sierra-Nevada Batholith) Magmas. *Am. J. Sci.* **1994**, *294*, 92–135. [[CrossRef](#)]
135. Piccoli, P.M.; Candela, P.A. Apatite in igneous systems. *Rev. Mineral. Geochem.* **2002**, *48*, 255–292. [[CrossRef](#)]
136. John, T.; Layne, G.D.; Haase, K.M.; Barnes, J.D. Chlorine isotope evidence for crustal recycling into the Earth’s mantle. *Earth Planet Sci. Lett.* **2010**, *298*, 175–182. [[CrossRef](#)]
137. Kusebauch, C.; John, T.; Barnes, J.D.; Klugel, A.; Austrheim, H.O. Halogen Element and Stable Chlorine Isotope Fractionation Caused by Fluid-Rock Interaction (Bamble Sector, SE Norway). *J. Petrol.* **2015**, *56*, 299–324. [[CrossRef](#)]
138. Kusebauch, C.; John, T.; Whitehouse, M.J.; Klemme, S.; Putnis, A. Distribution of halogens between fluid and apatite during fluid-mediated replacement processes. *Geochim. Cosmochim. Acta* **2015**, *170*, 225–246. [[CrossRef](#)]
139. Bellucci, J.J.; Whitehouse, M.J.; John, T.; Nemchin, A.A.; Snape, J.F.; Bland, P.A.; Benedix, G.K. Halogen and Cl isotopic systematics in Martian phosphates: Implications for the Cl cycle and surface halogen reservoirs on Mars. *Earth Planet Sci. Lett.* **2017**, *458*, 192–202. [[CrossRef](#)]
140. Sch’auble, E.A.; Rossman, G.R.; Taylor, H.P. Theoretical estimates of equilibrium chlorine-isotope fractionations. *Geochim. Cosmochim. Acta* **2003**, *67*, 3267–3281. [[CrossRef](#)]
141. Sharp, Z.D.; Barnes, J.D.; Fischer, T.P.; Halick, M. An experimental determination of chlorine isotope fractionation in acid systems and applications to volcanic fumaroles. *Geochim. Cosmochim. Acta* **2010**, *74*, 264–273. [[CrossRef](#)]
142. Pan, Y.M.; Fleet, M.E. Compositions of the apatite-group minerals: Substitution mechanisms and controlling factors. *Rev. Mineral. Geochem.* **2002**, *48*, 13–49. [[CrossRef](#)]
143. Penel, G.; Leroy, G.; Rey, C.; Bres, E. MicroRaman spectral study of the PO<sub>4</sub> and CO<sub>3</sub> vibrational modes in synthetic and biological apatites. *Calcif. Tissue Int.* **1998**, *63*, 475–481. [[CrossRef](#)]
144. Antonakos, A.; Liarokapis, E.; Leventouri, T. Micro-Raman and FTIR studies of synthetic and natural apatites. *Biomaterials* **2007**, *28*, 3043–3054. [[CrossRef](#)]
145. Pan, L.C.; Hu, R.Z.; Wang, X.S.; Bi, X.W.; Zhu, J.J.; Li, C.S. Apatite trace element and halogen compositions as petrogenetic-metallogenic indicators: Examples from four granite plutons in the Sanjiang region, SW China. *Lithos* **2016**, *254*, 118–130. [[CrossRef](#)]
146. Groves, D.I.; Vielreicher, N.M. The Phalabowra (Palabora) carbonatite-hosted magnetite-copper sulfide deposit, South Africa: An end member of the iron-oxide copper-gold-rare earth element deposit group? *Min. Depos.* **2001**, *36*, 189–194. [[CrossRef](#)]
147. Pan, Y.; Fleet, M.E. Composition of the apatite-group minerals: Substitution mechanism and controlling factors. In *Phosphates: Geochemical, Geobiological and Material Importance*; Kohn, M.J., Rakovan, J., Hughes, J.M., Eds.; Mineralogical Society of America: Washington, DC, USA; Volume 48.

148. Rasmussen, K.L.; Mortensen, J.K. Magmatic petrogenesis and the evolution of (F:Cl:OH) fluid composition in barren and tungsten skarn-associated plutons using apatite and biotite compositions: Case studies from the northern Canadian Cordillera. *Ore Geol. Rev.* **2013**, *50*, 118–142. [[CrossRef](#)]
149. Tartese, R.; Anand, M.; Barnes, J.J.; Starkey, N.A.; Franchi, I.A.; Sano, Y. The abundance, distribution, and isotopic composition of Hydrogen in the Moon as revealed by basaltic lunar samples: Implications for the volatile inventory of the Moon. *Geochim. Cosmochim. Acta* **2013**, *122*, 58–74. [[CrossRef](#)]
150. Barnes, J.J.; Franchi, I.A.; Anand, M.; Tartese, R.; Starkey, N.A.; Koike, M.; Sano, Y.; Russell, S.S. Accurate and precise measurements of the D/H ratio and hydroxyl content in lunar apatites using NanoSIMS. *Chem. Geol.* **2013**, *337*, 48–55. [[CrossRef](#)]
151. Candela, P.A. Toward a Thermodynamic Model for the Halogens in Magmatic Systems—An Application to Melt Vapor Apatite Equilibria. *Chem. Geol.* **1986**, *57*, 289–301. [[CrossRef](#)]
152. Jolliff, B.L.; Papike, J.J.; Shearer, C.K. Inter-Crystal and Intra-Crystal Ree Variations in Apatite from the Ingersoll, Bob Pegmatite, Black Hills, South-Dakota. *Geochim. Cosmochim. Acta* **1989**, *53*, 429–441. [[CrossRef](#)]
153. Coulson, I.M.; Chambers, A.D. Patterns of zonation in rare-earth-bearing minerals in nepheline syenites of the north Qoroq Center, South Greenland. *Can. Mineral.* **1996**, *34*, 1163–1178.
154. Eriksson, K.A. Sedimentation Patterns in the Barberton Mountain Land, South-Africa, and the Pilbara Block, Australia—Evidence for Archean Rifted Continental Margins. *Tectonophysics* **1982**, *81*, 179–193. [[CrossRef](#)]
155. Giebel, R.J.; Marks, M.A.W.; Gauert, C.D.K.; Marid, G. A model for the formation of carbonatite-phoscorite assemblages based on the compositional variations of mica and apatite from the Palabora Carbonatite Complex, South Africa. *Lithos* **2019**, *324*, 89–104. [[CrossRef](#)]